8

Synthesis of the Seismic Structure of the Greater Alaska Region: Subducting Slab Geometry

Gary L. Pavlis[1], Margarete A. Jadamec[2,3], Michael Everett Mann[4], Xiaotao Yang[5], Andrew John Schaeffer[6], Songqiao Shawn Wei[7], and Karen M. Fischer[4]

ABSTRACT

We utilized a normalized vote method to define common features in teleseismic, body-wave tomography models produced from the Alaska USArray data. The metric is used with three-dimensional visualizations to define subducting slab geometry. We observe the following features. (1) The eastern end of the slab downstream from the Yakutat microplate has a flap-like structure extending to 300–350 km depth that is bounded on the east by an edge consistent with rigid plate kinematics and on the west by a tear located downstream from the western limit of Yakutat rocks. (2) The geometry matches Slab2.0. (3) Below Slab2.0, the dip steepens to form a vertical structure that extends to the top of the mantle transition zone. Within the transition zone, the geometry changes from north to south dipping to form a lithospheric scale, recumbent fold connected to a lower-mantle structure located ~1,000 km south of the trench. (4) A previously unknown mantle structure extends eastward from the flat slab to an edge predicted by rigid plate kinematics suggesting it is an older section of the Pacific Plate emplaced before the Yakutat tear initiated. We propose a new kinematic model of subduction history in Alaska since 40 Ma consistent with the new data.

8.1. INTRODUCTION

8.1.1. Motivation and Scope

EarthScope data have revolutionized the community's understanding of the seismic structure and tectonic framework of the continental United States. From the beginning of 2015, the EarthScope Transportable Array (TA) transitioned from the lower 48 states to Alaska. Prior to EarthScope, the seismic coverage in Alaska was heavily focused on the southern part of the state where the seismicity rate is the highest in the country (Ratchkovski & Hansen, 2002a, 2002b). In the same way, the TA has revolutionized the understanding of crust and upper-mantle structure in the lower 48 states through uniform coverage with high-quality seismic records, and recent results from the TA in Alaska have revolutionized the understanding of the tectonics of Alaska and its adjacent areas. This chapter is one of a pair of chapters from the same group of authors in this monograph focused on two different, but related topics. This chapter focuses on upper-mantle structure constrained by body-wave tomography models and receiver function imaging and how the new data constrain the geometry of the subduction zone. Its

---

[1] *Department of Earth and Atmospheric Sciences, Indiana University Bloomington, Bloomington, IN, USA*

[2] *Department of Geology, University at Buffalo, Buffalo, NY, USA*

[3] *Institute for Artificial Intelligence and Data Science, University at Buffalo, Buffalo, NY, USA*

[4] *Department of Earth, Environmental, and Planetary Sciences, Brown University, Providence, RI, USA*

[5] *Department of Earth, Atmospheric, and Planetary Sciences, Purdue University, West Lafayette, IN, USA*

[6] *Geological Survey of Canada, Natural Resources Canada, Sidney, Canada*

[7] *Department of Earth and Environmental Sciences, Michigan State University, East Lansing, MI, USA*

Tectonics and Seismic Structure of Alaska and Northwestern Canada: EarthScope and Beyond, Geophysical Monograph 290, First Edition.
Edited by Natalia A. Ruppert, Margarete A. Jadamec, and Jeffrey T. Freymueller.

DOI: 10.1002/9781394195947.ch8
Companion website: www.wiley.com/go/Ruppert

companion chapter (Yang et al., this monograph) focuses on the structure of continental lithosphere constrained by surface-wave tomography using ambient noise cross-correlations and earthquakes, and teleseismic receiver function analyses for crustal thicknesses.

Prior to the digital age, a review chapter like this would have been limited to a literature review of publications. Today, as this chapter demonstrates, one can go further by directly comparing model estimates within a study region. The ease of access to the actual digital models authors used for their publications opens the door for more ways to independently evaluate interpretations of that data. We thus strove to separate objective observations from interpretations. The Results section focuses on geometric features that are objective observations. We defer all tectonic interpretations to the Discussion section where we present new ideas in the context of previous interpretations from the literature. The new results from EarthScope produced contradictions in much of the published literature we attempt to resolve with a new kinematic model for the past 40 Ma.

This chapter is a significant contribution for three reasons. First, a summary review of imaging results relevant to the subduction zone geometry from the Alaska TA deployment is a useful contribution to the community. Second, the vote map method we utilized here highlights major velocity anomalies shared by multiple tomographic models and provides new insights into the geometry and dynamics of the Alaska subduction system. In the Discussion section, we suggest multiple competing hypotheses that future investigators could use as a focus for their continued research in this area. Finally, we introduce a new kinematic model for the subduction history over the past 40 Ma that is the only model we have been able to produce to reconcile the new observations from EarthScope. We hope this new model can provide a basis for hypothesis-based future studies.

8.1.2. Tectonic Setting of the Aleutian–Alaska Subduction Zone

The Aleutian–Alaska subduction system is a major subduction zone (Bird, 2003; Hayes et al., 2018; Jadamec et al., 2018b) extending from approximately 196°W longitude to 135° W longitude (Bird, 2003; Hayes et al., 2018; Tozer et al., 2019). It delineates the northern tectonic boundary of the oceanic Pacific Plate (Bird, 2003; Hayes et al., 2018; Jadamec et al., 2018b; Müller et al., 2019; Plafker, Gilpin, & Lahr, 1994; Seton et al., 2020). The age of the oceanic crust on the incoming Pacific Plate (Figure 8.1) decreases from west to east along the length of the trench, ranging from 110 Ma near the western terminus of the trench (Aleutian–Kamchatka trench intersection) to 25 Ma at the eastern terminus of the subduction zone at the Fairweather Fault (Bird, 2003; Müller et al., 2019; Seton et al., 2020; Tozer et al., 2019). Offshore, the isochrons on the Pacific Plate (Figure 8.1) vary from subparallel to subperpendicular in their orientation with respect to each other and with respect to the trench (Engebretson et al., 1984, 1985; Müller et al., 2019; Seton et al., 2020). That geometry is widely recognized as evidence of multiple orientations of relic mid-ocean ridges and seafloor spreading directions (Engebretson et al., 1984, 1985; Fuston & Wu, 2020; Haeussler et al., 2003; Wallace & Engebretson, 1984). The modern location of the relic oceanic lithosphere beneath Alaska and northwestern Canada is an active area of research with large-scale tectonic implications (Engebretson et al., 1984, 1985; Fuston & Wu, 2020; Haeussler et al., 2003; Madsen et al., 2006; Wallace & Engebretson, 1984).

The laterally extensive Aleutian–Alaska subduction zone can be separated into two broad tectonic settings (Bird, 2003; Müller et al., 2019; Plafker, Gilpin, & Lahr, 1994; Seton et al., 2020; Tozer et al., 2019). West of approximately 170° W, the Aleutian–Alaska subduction zone is characterized by ocean–ocean subduction at the trench, with the oceanic Pacific Plate subducting under the oceanic lithosphere below the Bering Sea (Bird, 2003; Hayes et al., 2018; Müller et al., 2019; Seton et al., 2020; Tozer et al., 2019). This oceanic-oceanic segment has traditionally been referred to as the Aleutian subduction zone. East of approximately 170° W, the Pacific Plate subducts primarily under the amalgamated Alaskan continental lithosphere (Bird, 2003; Hayes et al., 2018; Jadamec et al., 2013; Moore & Box, 2016; Müller et al., 2019; Plafker, Gilpin, & Lahr, 1994; Seton et al., 2020; Tozer et al., 2019). This ocean–continent segment is commonly referred to as the Alaska subduction zone. The subduction zone experiences significant earthquakes and deformation across the entire margin. The Alaska subduction zone segment was the site of the M_w 9.2 Great Alaska Earthquake (Christensen & Beck, 1994; Plafker, Gilpin, & Lahr, 1994) and contains the most active exhumation and mountain building in North America (Enkelmann et al., 2010; Fitzgerald et al., 1995; Jadamec et al., 2013).

The eastern terminus of the Alaska subduction zone is best described as a zone of deformation rather than by a distinct point (Figure 8.1). At its easternmost end, the Alaska subduction zone intersects the Fairweather–Queen Charlotte transform fault system at nearly a right angle, forming a plate boundary corner (Bird, 2003; Elliot & Freymueller, 2020; Jadamec & Billen, 2012; Plafker, Gilpin, & Lahr, 1994). The deformation in the corner is expressed as a three-dimensional

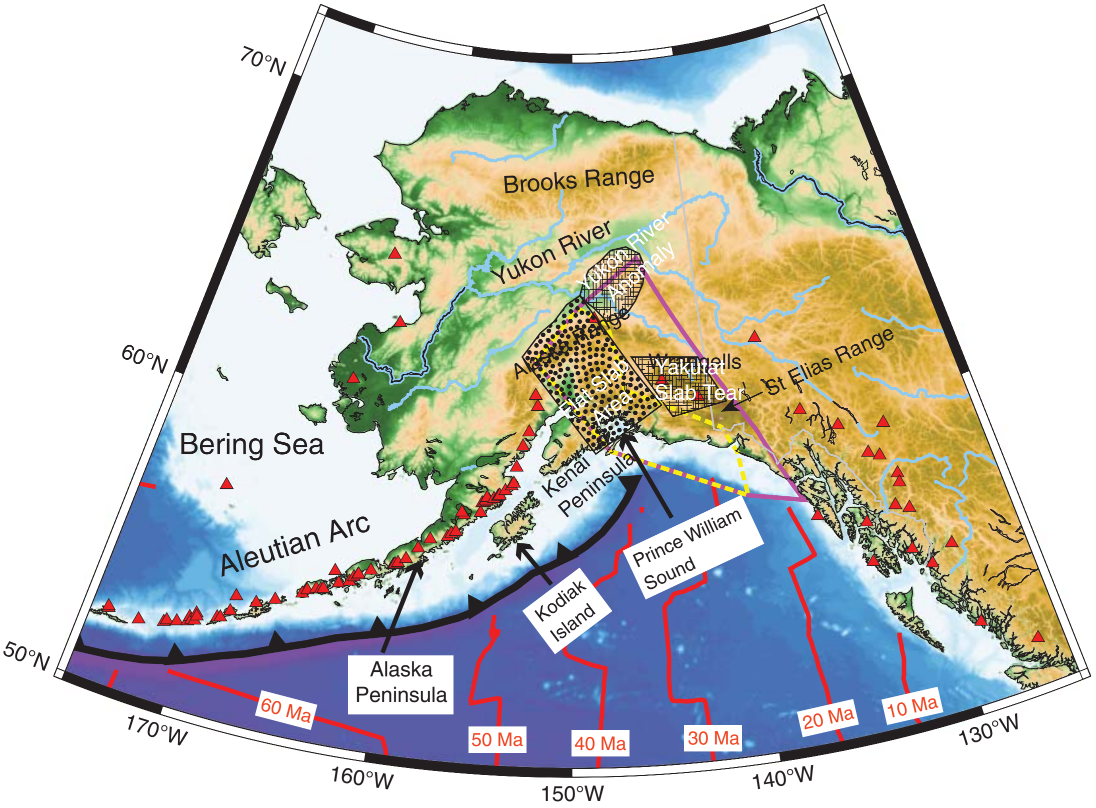

Figure 8.1 Tectonic setting of the Alaska subduction zone. The base map is a Lambert conic, conformal projection with a topography colored by elevation, coastline in black, and major rivers in light blue. Geographic features referenced in the text are labeled with black letters. Red triangles indicate locations of Holocene volcanoes from the database of Global Volcanism Program (2022). Colored contours are depth to the top of the subducting slab based on Slab 2.0 (Hayes et al., 2018) with contour colors illustrated by the legend. The location of the trench is shown as a heavy black line with teeth pointing downdip. The dashed yellow and solid magenta polygons are the estimated outlines of the Yakutat microplate from Eberhart-Phillips et al. (2006) and G. L. Pavlis et al. (2019), respectively. Ocean age contours are displayed with heavy red lines with age labels. Hatched areas with white labels are subduction zone features discussed extensively in the text. The companion website contains a layered pdf version of this figure. It contains additional features and allows one to turn elements on and off to better show overlapping features.

(3-D) structure that G. L. Pavlis et al. (2019) argue has two key features: (1) crustal faults splay into what they call the "middlebuster" geometry and (2) the crust and mantle portions of the lithosphere appear to be moving with different trajectories. The corner is spatially correlated with uplift of the St. Elias Range that has one of the highest uplift rates in the world (Enkelmann et al., 2010). The Yakutat microplate is actively subducting–colliding into the broader eastern terminus zone (Eberhart-Phillips et al., 2006; Ferris et al., 2003; G. L. Pavlis et al., 2019; Plafker, Gilpin, & Lahr, 1994). The subducting plate downstream from the trench west of the outcrop area of Yakutat rocks is characterized by flat slab subduction (Brocher et al., 1994; Hayes et al., 2018; Jadamec & Billen, 2010; Lallemand et al., 2005; Nayak et al., 2020; Veilleux & Doser, 2007; Zhao et al., 1995), oblique convergence (DeMets et al., 1994), and varying degrees of coupling with the overriding plate (Elliot & Freymueller, 2020; Fitzgerald et al., 2014; Haynie & Jadamec, 2017; Kalbas et al., 2008). East of the flat slab region, earlier studies have suggested a short (~100 km) east–northeast-dipping slab segment beneath the Wrangell Mountains [e.g., Wrangell slab (Jadamec & Billen, 2010; Stephens et al., 1984)] and a discontinuity at depth between the northeast-dipping Wrangell slab and the larger Aleutian–Alaska slab (e.g., Fuis et al. 2008; Zhao et al. 1995). Prior to EarthScope, the nature of the subsurface slab geometry east of the flat slab region and north of the offshore Yakutat microplate was poorly constrained. Arguably, one of the most important discoveries from the USArray deployment came from illuminating the structure in this less understood area.

8.1.3. Timing Constraints on Mesozoic to Cenozoic Subduction History

To understand the current geometry of the Aleutian–Alaska subduction zone, it is important for all readers to have a basic understanding of the geologic history of the subduction system. In reviewing the published imaging work with TA data, we were struck by how little the time history was considered in interpretations of these papers. Given that prior to EarthScope most of what we knew about the tectonics of Alaska came from the rock record, that omission is problematic. Consequently, we review some key issues here to better frame our interpretations made later in the chapter.

We utilize a graphical tool borrowed from petroleum geology called an event chart in Figure 8.2. The figure highlights key tectonic events important for understanding the 4D history that shaped what we see today. The item numbers below are the same as those used as tags for events in Figure 8.2.

1. From the Paleozoic to mid-Mesozoic, Alaska did not exist in anything like its present form. Plafker and Berg (1994) argue that all of the crust of southern Alaska at that time either did not exist or was located hundreds to thousands of kilometers southeast of the present location. Northern Alaska, in contrast, had a very different history. Plafker and Berg (1994) suggest that during the mid-Mesozoic the older crust north of the Alaska Range was rotated into its current position from what is now the northwest corner of Canada. Although that rift model for the translation of northern Alaska to its present position has been widely accepted for decades, McClelland et al. 2021) recently suggested that northern Alaska moved to its present position by strike-slip motions on the Canadian Arctic Transform Systems. A key point is that both models indicate that northern Alaska and southern Alaska lithosphere have radically different origins. The boundary between the two regions is a mid-Mesozoic suture commonly associated with rocks of the Kahiltna Group (Hults et al., 2013) of the Alaska Range and the Gravita assemblage in southeastern Alaska (T. L. Pavlis et al., 2019). The crust south of that suture is widely accepted to be an ensemble of exotic terranes assembled from fragments of crust rafted in since mid-Mesozoic (e.g., T. L. Pavlis et al., 2019).
2. The period from the Cretaceous to no later than about 40 Ma (Doubrovine & Tarduno, 2008; Engebretson et al., 1984) is characterized in Figure 8.2 as the Kula subduction time. A key perspective to have on this period is to remember that the word Kula is a geologic play on words. Kula means ‘all gone’ in the Tlingit (an indigenous people from southeast Alaska and western British Columbia) language. The primary direct constraints on the Kula Plate are a few remnant magnetic anomalies in the Gulf of Alaska as shown in Figure 8.1. Other information about the Kula Plate comes mostly from the rock record, dominated by the timing and petrology of volcanic rocks along the margin from Alaska through the Pacific Northwest of the United States (e.g., Haeussler et al., 2003 or Wells et al., 2014). The detailed history of the Kula subduction period has been the subject of a decades-long debate for many reasons. What seems indisputable is that during this time one or more mid-ocean ridge systems were subducted along the margin between Alaska and the Pacific Northwest. The exact geometry of the ridge system, however, is poorly constrained because most of Kula is “all gone.” Magnetic anomalies in the Gulf of Alaska that are universally assigned to the Kula–Pacific and Kula–Farallon Ridge are the anchor for all reconstructions such as that of Fuston

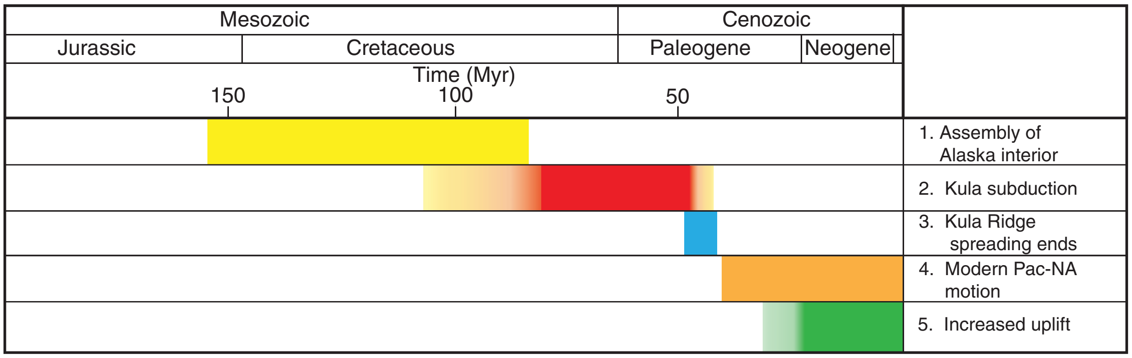

Figure 8.2 Tectonic event chart. The chart uses a linear timescale shown at the top along with major geologic time periods. Major events discussed in the text are given short titles on the right. Number tags are the same as item numbers explained in the Discussion section. The time spans of the events are shown as colored bars. Intervals with poorly defined edges are illustrated with color gradients. See the text for sources used to construct this chart.

and Wu (2020). A debate exists at present for the existence of the idea of a 'Resurrection Plate' introduced by Haeussler et al. 2003). That model adds an 'all gone' plate they call the Resurrection Plate, and a secondary ridge system that Haeussler et al. argue was subducted under western North America during this period. We return to the implications of the Kula history later, but the key point, for now, is that there is little question that the Kula–Farallon system formed a continuous subduction zone from Alaska to at least northern Mexico during this period. That history is preserved in the mantle under the entire northern Cordillera but is complicated by a later, major event we describe next. It also had to have left one or more remnants of slab windows under western Canada and the Pacific Northwest that are an inevitable consequence of ridge subduction (e.g., Madsen et al. 2006; Thorkelson, 1996). It should also be noted that the composite terrane often referred to as the Wrangellia superterrane or Insular superterrane was assembled by the end of this period (e.g., T. L. Pavlis et al. 2019). Controversy remains about the amount of strike-slip motion on the Denali Fault that has transported the composite terrane since its assembly in the Mesozoic (Regan et al., 2020).

3. Starting around 56 Ma (anomaly 25n) and ending somewhere between 48 Ma (anomaly 21n) and 40 Ma (chron 18r), the Kula/Resurrection plate(s) "died" and began moving with the Pacific Plate [e.g., Haeussler et al. (2003), Madsen et al. (2006), or Wells et al. (2014)]. The east–west oriented magnetic anomalies that are still present in the Gulf of Alaska are the remnant of the part of the Pacific Plate generated by Kula-Pacific ridge. A key point we return to below is that plate kinematics require that Kula/Resurrection lithosphere is a major part of the slabs imaged by the tomography models considered in this chapter. We emphasize "required," because Kula lithosphere must be there based on plate tectonic fundamentals. An important question is if it is being imaged reliably by current methods.
4. By around 42 Ma, the Pacific Plate had undergone a major change in direction relative to North America. Since that time Pacific–North America relative motion has been similar to the present motion. The present motion has helped shape the western boundary of North America into the two long transform fault systems of the San Andreas and Queen Charlotte Fault systems. The post-40+ Ma history is critical to understanding the current geometry of the Alaska subduction system as at least 2,000 km of oceanic crust has been subducted along a nearly constant trajectory during that period. A major complication is the Yakutat microplate. The rock record and plate kinematics provide overwhelming evidence that the crust of the Yakutat microplate began a journey northward along with the Pacific Plate near the beginning of this period. The details of how the Yakutat microplate was sliced from the margin around that time, however, are not yet completely clear. The older, classic model of Bruns (1983) placed the origin of the Yakutat microplate in northern California, but recent work by Wells et al. (2014) provides evidence that during this period, at least, the Yakutat microplate was located offshore from Washington state. What is not clear is what tectonic processes plucked this block of crust from the margin to start its northward journey to the present location in southeast Alaska. A key unexplained detail is the discovery by Christeson et al. (2010) of a vertical offset in the crust–mantle boundary along the Transition Fault at the southern edge of the Yakutat microplate. That structural relationship suggests strongly that boundary had a history of strike-slip motion that is not consistent with the current, limited motion shown by GPS motion (J. L. Elliott et al., 2010; G. L. Pavlis et al., 2019). That is important for this chapter because there is a potentially unresolved history of strike-slip motion on the Transition Fault in the past. When that happened and the sense of motion would determine whether any fragment of that history is preserved anywhere in the mantle.
5. Modern plate models all indicate that Pacific–North American plate motion has been similar to the present for around 40 Myr. That geometry has subducted most of the Kula Plate and transported the Yakutat microplate to its current position at the eastern edge of the Aleutian–Alaska subduction zone. A long-standing controversy in Alaskan geology is when the system transitioned from normal subduction to the current flat slab geometry in central Alaska. The strongest constraints on the answer to that question come from the volcanic history of the margin. Finzel et al. (2011) compiled data to address this question. The volcanic record shows rocks with ages older than 40 Ma span the entire margin. Their compilation also shows a gap in volcanic rocks in the age range of 40 and 30 in the vicinity of the modern Wrangell volcanic field. Recent work (Berkelhammer et al., 2019; Trop et al., 2021) indicates that the Wrangell volcanic field initiated around 30 Ma while the compilations of Finzel et al. (2011) indicate that volcanism ceased in the modern flat slab region around the same time. Finzel et al. (2011) also used additional proxies from geochronology to conclude that the slab has been subducting at a shallow angle

since the initial subduction in late-Eocene–early Oligocene time. We label this stage as "Increased uplift" in Figure 8.2. The color gradient on the bar emphasizes the timing of "increased uplift" is not exact.

8.1.4. Study Area

To organize the discussion below, we divide the study area into four subregions based on subsurface structures we observe within them. From west to east, we use the following terms: (1) the Aleutian–Alaska Peninsula region, (2) the Kodiak–Prince William Sound region, (3) the Yakutat–Wrangell region, and (4) the Yukon region.

The Aleutian–Alaska Peninsula region comprises the westernmost part of the study area. It spans the ocean–ocean to ocean–continent subduction transition (approximately 170° W longitude) eastward along the Alaska Peninsula to the western tip of Kodiak Island (Figure 8.1). Here, the Wadati–Benioff zone seismicity indicates the Pacific slab dips moderately to the northwest (Hayes et al., 2018; Jadamec et al., 2018b; Lallemand et al., 2005), but the depth extent and continuity of the slab below the depth of seismicity was poorly known prior to EarthScope. Much of what was known previously about the large-scale structure of the Aleutian–Alaska slab came from models of slab geometries for all of the major subduction zones on Earth (e.g., Gudmundsson & Sambridge, 1998; Hayes et al. 2012; Syracuse & Abers, 2006). In addition, more localized seismic-kinematic models examined the connection of the upper slab to the transition zone in the central and western Aleutians (e.g., Boyd & Creager, 1991). A 3-D comparison of the earlier models of Aleutian–Alaska slab geometry can be seen in Movies 2 and 3 from the global slab geometry movie collection of Jadamec et al., (2018a, 2018b).

The Kodiak–Prince William Sound region spans the area from Kodiak Island to Prince William Sound. It is characterized by an eastward change from a moderately northwest-dipping slab to a north–northwest–dipping flat slab (Brocher et al., 1994; Hayes et al., 2012; Jadamec & Billen, 2010; Jadamec et al., 2018b; Lallemand et al., 2005; Ratchkovski & Hansen, 2002b; Veilleux & Doser, 2007; Zhao et al., 1995) (Figure 8.1). The geometry of the upper part of the slab in this section has been known for decades on the basis of intermediate-depth earthquakes. Seismicity data were a primary constraint used to construct the Slab2.0 (Hayes et al., 2018) and the earlier Slab1.0 (Hayes et al., 2012) surfaces in the Alaska region used in this chapter and many others. In addition to the global slab models of Slab1.0/Slab2.0, earlier seismic studies (Zhao et al., 1995) and geodynamic modeling studies (Jadamec & Billen, 2010, 2012) provided slab surface models for this region. More recently, G. L. Pavlis et al., (2019) created a regional scale set of surfaces using Slab 1.0 merged with higher resolution results from the STEEP study area in southeast Alaska. Prior to the TA deployment in Alaska, however, the deeper structure was poorly constrained due to the sparse station coverage outside of seismically active areas. Structures at greater depths than the published slab interface models should thus be viewed as an EarthScope discovery. The established geometry from Slab2.0 is illustrated by the contour lines in Figure 8.1.

The Yakutat–Wrangell region spans the eastern side of Prince William Sound to the Fairweather Fault and encompasses the colliding Yakutat microplate zone (Eberhart-Phillips et al., 2006; Mann et al., 2022; G. L. Pavlis et al., 2019; Yang & Gao, 2020). The BEAAR and MOOS projects (Kim et al., 2014) produced important constraints on the geometry of the zone between the Yakutat–Wrangell and Kodiak–Prince William sections, but coverage was limited to a two-dimensional (2-D) profile near the highways in central Alaska. The STEEP project produced new constraints on the geometry of southeast Alaska from the analysis of passive and active seismic data (Bauer et al., 2014; Christeson et al., 2010; Worthington et al., 2008; Worthington et al., 2012), but coverage was limited to the vicinity of Yakutat crust and did not include the Wrangells or the Yukon, which was an EarthScope frontier. Eberhart Phillips et al. (2006) used local earthquake tomography to image most of southern Alaska, but the resolution in the mantle of the Yakutat Section was poorer because of limited mantle earthquakes and station coverage. Early seismic models used the limited amount of seismicity in the vicinity of the Wrangell volcanics to constrain a moderately northeast dipping short slab known as the Wrangell slab (Stephens et al., 1984). However, due to lack of coverage and the decrease in seismicity, there was uncertainty how the Pacific–Yakutat slab connected to the Wrangell slab (Zhao et al., 1995). The 3-D geodynamic and seismic synthesis work in Jadamec and Billen (2010, 2012) produced two end-member slab geometries that contained a continuous flat slab beneath south-central Alaska at shallower depths, but a variable slab depth extent, with a shorter (~90–100 km) northeast dipping slab beneath the Wrangell mountains. The slab model using a shorter slab segment beneath the Wrangell volcanics (Slab_E115) provided the best fit when used in geodynamic models and compared against independent geologic observations (Jadamec & Billen, 2010, 2012), with movies of the slab shapes in Jadamec et al. (2018b). An implication of the shorter slab beneath the Wrangell volcanics, and/or the lack of seismic signature where the Pacific–Yakutat–Wrangell slabs meet, is that part of a slab segment may be missing, possibly torn or detached, or that part of the slab junction was never fully connected. Plate kinematics demand that the eastern limit of the modern subduction system lies downstream from the modern outcrop of the Yakutat microplate. The fundamental reason is that Pacific–North America plate motion has not varied strongly in the last 40+ Ma (e.g., Doubrovine & Tarduno, 2008). That motion has created the Queen Charlotte Fault system running from southern British Columbia to southeast Alaska that terminates at a tectonic corner near Mt. St. Elias as discussed above. North of that boundary lithospheric subduction is required by plate kinematics but is complicated by ambiguities in the poorly constrained relative motion of the Yakutat microplate (e.g., G. L. Pavlis et al. 2019).

The Yukon region is the easternmost region examined in our analysis. We define the tectonic-physiographic Yukon region as the part of eastern Alaska and northwestern Canada bounded on the west by the Fairweather–Queen Charlotte transform fault system and on the east by the Mackenzie Mountains. At depth, we define this area as the region of the upper mantle east of all feasible Yakutat plate edges defined by plate kinematics for the past 40 Ma based on the models of G. L. Pavlis et al. (2019). That constraint is important because it means any mantle structure in this area is most likely older than the 40+ Ma history of strike-slip motion of Pacific–North America that has produced the Queen Charlotte Fault system in western British Columbia.

8.2. DATA

This chapter analyzes seismic imaging results from EarthScope for the Alaska portion of the Aleutian–Alaska subduction zone, east of 164° W to the western part of the Yukon Territory, and to a depth of the order of 800 km. That means the volume extends through the transition zone to the top of the lower mantle (Figure 8.1). We collected seismic models from six studies for this synthesis, including four body-wave tomographic studies producing five different velocity models and two receiver function studies providing three seismic discontinuity volumes. Two of the six were obtained from Products (2021) and the others were obtained directly from the authors. Key features of these data are summarized in Table 8.1.

8.2.1. Teleseismic Body-Wave Studies

Since the objective of this chapter is to define the geometry of the slab in the upper mantle, our primary data source was tomography models that utilized teleseismic body waves. We obtained models in digital form from four sources:

1. *Burdick et al. (2017)*. That paper used the same technique used as a series of model updates (Burdick et al., 2008, 2009, 2010, 2012, 2014) through the years of the TA deployment in the lower 48 states. The difference in their 2017 paper was the addition of early

Table 8.1 List of seismic imaging results used for this synthesis. δV_p and δV_s refer to perturbations of P-velocity and S-velocity models, respectively.

Seismic model		Data	Property	Method(s)
Body-wave models				
1	Burdick et al. (2017)	ANF P teleseismic P picks	δV_p	Li et al. (2006)
2	Jiang, Schmandt, Ward, et al. (2018)	Rayleigh Wave dispersion	δV_s	Jiang, Schmandt, Hansen, et al. (2018)
		S picks		
3	Guo et al. (2019)	ANF P teleseismic P picks	δV_p	Zhao et al. (1995)
		AK local P picks		Zhao et al. (2012)
4a,b	Esteve et al. (2019); Esteve et al. (2020)	teleseismic P and S time (multichannel correlation)	$\delta V_p, \delta V_s$	Lou et al. (2013); VanDecar et al. (1995)
Receiver function imaging				
1	Mann et al. (2022)	P–S receiver functions	$\delta V_p, \delta V_s$	Bostock et al. (2001)
2	Bauer et al. (2014)	S–P receiver functions	S–P amplitude	Kumar et al. (2005)

Notes: In the layered graphic files found on the companion website, the seismic models numbered in the table are labeled according to the following nomenclature. Body-wave models: 1, MIT15; 2, Jiang, Schmandt, Ward, et al. 2018; 3, Gou et al. 2019; 4a, NWCAN_P; 4b, NWCAN_S. Receiver function imaging: 1, Mann et al. 2022; 2, Bauer et al. 2014 STEEP, Bauer et al. 2014 Regional.

arrival time data from the TA Alaska deployment and the densification of the model grid in Alaska. This is the lowest resolution model because it used an early set of data from the Alaska TA deployment that was smaller than any of the other models. It is unique, however, as a combined global and regional inversion. It would have been preferable to use the recent model by Boyce et al. (2023) that is an extension of MIT15 with major improvements in Canada. That model, however, was not available at the time we did this analysis.

2. *Jiang et al. (2018)*. This model was produced from the joint inversion of two data sets: (1) Rayleigh-wave phase velocity measurements inverted into a series of phase velocity maps and (2) 86,000 S-wave residuals produced by an automated, multichannel waveform correlation method. Resolution tests in their paper suggest that this model has a resolution of the order of ~150 km in the upper mantle with poorer resolution in and below the transition zone where the model is constrained only by the body-wave data.
3. *Guo et al. (2019)*. This model was computed using P-wave arrival time data from three sources: (1) local earthquake picks from the Alaska Earthquake Center catalog, (2) P-wave picks from Alaska stations tabulated in the ISC catalog from 1977 to 2014, and (3) EarthScope's Array Network Facility (ANF) P-wave data picks from 2015 to 2017. They inverted these data for P-wave perturbations using the method of Zhao et al. (1995, 2012). They also applied the anisotropic inversion method of Wang and Zhou (2008, 2013) in an independent inversion including anisotropic parameters. We do not show any of their anisotropic inversion results in this paper for consistency with the other models. The anisotropic model converted to a format viewable in paraview in relation to other models can be downloaded from the companion website.
4. *Esteve et al. (2019, 2020)*. They estimated P- and S-wave models from teleseismic P- and S-wave residuals measured by multichannel cross-correlation as implemented in the AIMBAT software of Lou et al. (2013). The data and coverage of these models are different from all the others used for this paper. Their study focused on northwest Canada and only used EarthScope TA and Alaska stations east of 146° W. On the other hand, they also processed data from a number of temporary deployments in southeast Alaska and northwestern Canada not used by other authors. The limited aperture and highly irregular coverage outside the TA footprint make the resolution of this model more irregular. In addition, the western edge of these models is located inside the highest resolution area of the other models that were focused on the TA deployment. Figure S1 of the companion website illustrates that geometry.

8.2.2. Receiver Function Studies

In addition to the body-wave tomography models, we utilize two sets of receiver function imaging results:

1. The P receiver function inversion profile results from Mann et al. (2022) were used. This study has the highest resolution of any imaging result we used, but is limited in coverage to a 2-D profile through the Wrangells.
2. We used two S receiver function image volumes from Bauer et al. (2014). One is a higher-resolution image centered approximately on Wrangell St Elias National Park, and the other is a regional model. The latter suffers from irregular broadband instrument coverage that characterized the area before the TA deployment, but was included as there is currently no comparable, published 3-D S to P conversion image volume.

Readers who are not experts in seismic imaging should recognize that receiver function images provide a different, complementary picture of Earth's interior. Receiver function images are more properly called scattered wave images as they are derived by wavefield processing of converted phases. The results we show here from Mann et al. (2022) used P to S conversions while the image volumes from Bauer et al. (2014) are based on S to P conversions. The analysis methods for these two sets of results also differ. Mann et al. (2022) use an inversion technique to form an image similar to velocity perturbations computed by seismic tomography methods. Bauer et al. (2014) used a version of common-conversion point stacking to produce 3-D image volumes that are more akin to a normal-moveout-corrected seismic reflections section. A key point is both highlight discontinuities while tomography images outline bigger scale regions of wave speed variation.

8.3. METHODS

8.3.1. Data Format

A fundamental challenge in any review of published earth models like this is how to compare the results. Before the widespread use of electronic supplements and downloadable data products like the EarthScope/IRIS Earth Model Collaboration (Products, 2021), what one could do was limited to figures in published papers and the irregular coverage that automatically creates. To use the digital data, one of the biggest initial challenges was digesting the wide range of incompatible formats and geometries used to define the 3-D objects that define a particular 'result.'

To address this issue, we created a framework set of 3-D objects based on an earlier approach that was developed to synthesize results from the STEEP project (G. L. Pavlis et al., 2019). The data supplement in G. L. Pavlis et al. (2019) contains a number of georeferenced, 3-D objects that gave us a background framework for some elements of this study. In particular, their model for the crust–mantle boundary, the top of the subducting slab, and kinematic predictions on the eastern extent of the subducting (Yakutat) lithosphere provided useful anchors. For that reason, we chose to map all the earth models we assembled into the coordinate system used by G. L. Pavlis et al. (2019).

8.3.2. Graphical Comparison

Our first approach to comparing results was a qualitative method that is an obvious starting point: direct graphical comparison. We used two forms of graphics that fit this description: (1) conventional cross-section and horizontal slice maps at common places in different models and (2) fully 3-D visualizations using animated slicing, volume visualization, and tricks of turning features on and off. Readers unfamiliar with the use of 3-D visualization in research should understand that no matter the method all such work has two phases: exploration to comprehend the geometry and presentation to try to explain what you see to others. The first is impossible to completely convey or even recreate, but is the reason 'graphical comparison' was step 1 of our analysis. This chapter is step 2. Readers with strong interest should consider viewing these data with paraview using files on the companion website to create a personalized, early exploration to fully comprehend the fully 3-D geometry of this subduction zone.

All the cross-section figures below are conventional graphics. They provide one view of a multilayered problem. That is, our objective was to understand what features were common among a suite of multiple earth models. In our early exploration, we sliced the different results along common planes and compared the results visually. We preserved some of that in figures on the companion website. There you will find layered graphics files that slice all the models we examined through the same planes as cross-section figures below. Readers are encouraged to examine those figures to objectively evaluate the validity of the vote map results described in the next section. The conventional, cross-section figures below are centered on vote map data as a useful summary of the results.

8.3.3. Vote Maps

For this chapter, we developed a version of a voting metric to quantitatively compare the models. This basic approach has been used previously to quantitatively compare global tomography models (e.g., Shephard et al., 2017). Shephard et al. (2017) used vote maps to track slabs focusing on deeper structures in the lower mantle. An issue faced in a regional synthesis like this that is not faced in a global synthesis, however, is that the models we examine do not all have the same coverage volume. The actual coverage counts with the study area are illustrated in Figure S2 of the companion website. Consequently, a simple counting mechanism like that used by Shephard et al. (2017) is not sufficient. We instead use a normalized vote computed as described in detail below. The focus of this chapter is the geometry of subducting slabs in the Alaska region. Our approach assumes that slabs can be detected in body-wave tomography models as high-velocity anomalies in the mantle.

The vote mapping algorithm we use is defined by the following steps:

Step 1: For each model we immediately discard all cells with negative velocity perturbations (lower velocities than the surroundings).

Step 2: All of the body-wave models we used for this chapter had zero for grid cells with null coverage. From histograms, we established a different floor for points we treated as a null. That was required because we used interpolation into a common grid system (Fan et al. 2006) to resample all the models on a common reference grid. Floor values we used where 0.025, 10^{-3}, 10^{-5}, and 10^{-6} or the models of Jiang, Schmandt, Ward, et al. (2018), Guo et al. (2019), Esteve et al. (2019), and Burdick et al. (2017), respectively. All such points with a positive value less than the threshold were treated as invalid and not counted in computing the vote map field.

Step 3: With each model we sorted the remaining positive values and computed a threshold value for which 25% of the values were below that threshold. We then zeroed those small values along with the negative values. We discarded the smallest values because they are subject to larger relative uncertainty and would thus be more prone to define the wrong sign of the local perturbation. We experimented with a range of percentages around that value and found 25% was a reasonable, round number choice.

Step 4: We constructed a structured grid using a descendent of the georeferenced grid geometry of Fan et al. (2006). We will refer to this as our "vote map field." At each grid point of the vote map field, we interpolate the positive filtered version of each earth model. Nonzero interpolated values were given a score of 1 and zero values were assigned a score of 0. At each cell, we also counted the number of models, N_{valid}, not marked invalid. We then store a computed normalized vote of $\frac{N_+}{N_{\text{valid}}}$ where N_+ is the count of models where the filtered value was nonzero.

8.4. RESULTS

The results for each region are described in the following sections. The results for the Yakutat–Wrangell region are presented first, followed by the results for the Kodiak–Prince William Sound region, the Alaska Peninsula–Aleutian region, and lastly the Yukon region. Figure 8.3 is a useful starting point. It shows eight depth slices through the vote map results in 100 km intervals. Figure 8.4 shows the location of seven cross-sections (AA'–GG') that are plotted in Figures 8.6–8.12. Notice all but sections AA' and BB' have a northeast trend that is approximately in the direction of relative North America–Pacific Plate motion.

The cross-sections in this monograph are conventional figures appropriate for printing as a simple, printable file. Readers are encouraged to also view the expanded form of all the cross-section figures on the companion website. Each of the cross-section figures has a layered version indexed by figure number in the master paper. The layers show slices through all of the models that were used to create the vote map field in identical planes. The layers provide a way for readers to independently evaluate our observations using a simple visualization trick of turning different layers on and off.

Note that the geometry we infer rapidly varies enough along strike that it is challenging to fully comprehend the geometry with a reasonable number of cross-sections. Thus, although this section will focus on the static slices, we urge the reader to examine the animations and 3-D PDF representations found on the companion website. The cross-section figures in the monograph can be thought of as snapshots from one of the two animations. We also supply data files of all the models and the vote map data in a common coordinate system for interactive visualization with Paraview.

8.4.1. Yakutat–Wrangell Region

Figures 8.5, 8.6, and 8.7 show vote map sections through the Yakutat–Wrangell region for cross-sections AA', BB', and DD', respectively. Observations we make from cross-sections AA', BB', and DD' in the Yakutat–Wrangell region are:

1. At shallow depths the slab dip matches the Moho model from G. L. Pavlis et al. (2019) as far north as the edge of the coverage provided by the STEEP data. The new results of Mann et al. (2022) highlighted in Figure 8.5 and all the tomography models indicate that the slab steepens sharply around the southern edge of the Wrangell volcanic field.
2. The 2-D section from Mann et al. (2022) shows a low-velocity body that terminates at a depth of 110 km. They interpret this low velocity as subducted crustal material. That interpretation is consistent with the geometry of the Moho inferred from STEEP data by G. L. Pavlis et al. (2019) that is illustrated in all three figures, but extends what was known to reveal the change in the dip of the slab at the northern limits of the STEEP data.
3. The tomography models indicate that the subducting Yakutat slab extends much deeper than what was imaged by Mann et al. (2022). The models show some variations, but the vote map results and individual model sections seen in Figures 8.5 and 8.7 show that the slab anomaly disappears between a depth of 300 and 350 km. Additional perspectives on that geometry can be obtained from the map views in Figure 8.3. The geometry of the high-velocity body seen with the vote map image is most clearly seen in Figure 8.7. It fades away east of that section and merges into a more complex structure west of the section illustrated in Figures 8.5 and 8.7.
4. Figure 8.3 shows that the eastern extent of the slab is consistent with the geometry predicted from plate kinematics by G. L. Pavlis et al. (2019) and inconsistent with the widely used polygon from the paper by Eberhart-Phillips et al. (2006). The implications of that observation are important but deferred to the Discussion section.
5. The results are convergent in showing the slab tears at a position centered around the southwest edge of the Wrangell volcanic field. Downstream from the tear point the western side of the slab defines the well-known flat slab region. To the east the slab forms a structure seen best in Figure 8.7. The vote map result suggests a separation of the high-velocity body along the tear. The western edge of the Yakutat section could be described as butting against a broad, high-velocity body under central Alaska.
6. The models are convergent in showing a second high-velocity body north of the Denali Fault whose existence was unknown prior to EarthScope. Figure 8.3 shows that anomaly is continuous with the deeper slab seen in central Alaska at transition

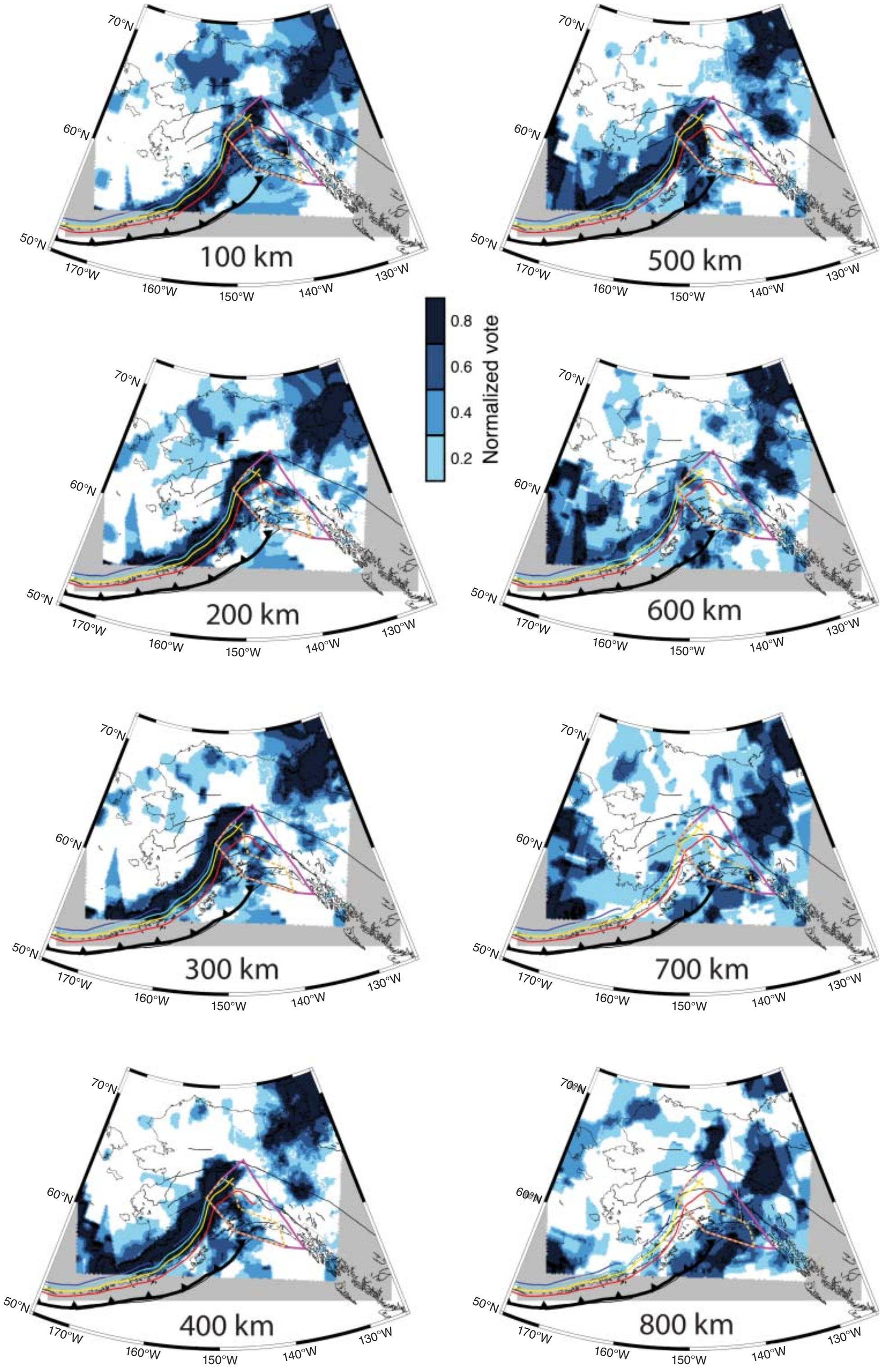

Figure 8.3 Constant depth slices of vote map data volume. Contours of Slab2.0 are as in Figure 8.1, which is a reference for the color scale. The map projection and region are the same as Figure 8.1. The depth of each slice is shown on each frame. We show two polygons that have been suggested for the map limits of lithosphere linked to the Yakutat microplate. The solid magenta polygon is that developed by G. L. Pavlis et al. (2019). The yellow dotted line shows that from Eberhart-Phillips et al. (2006).

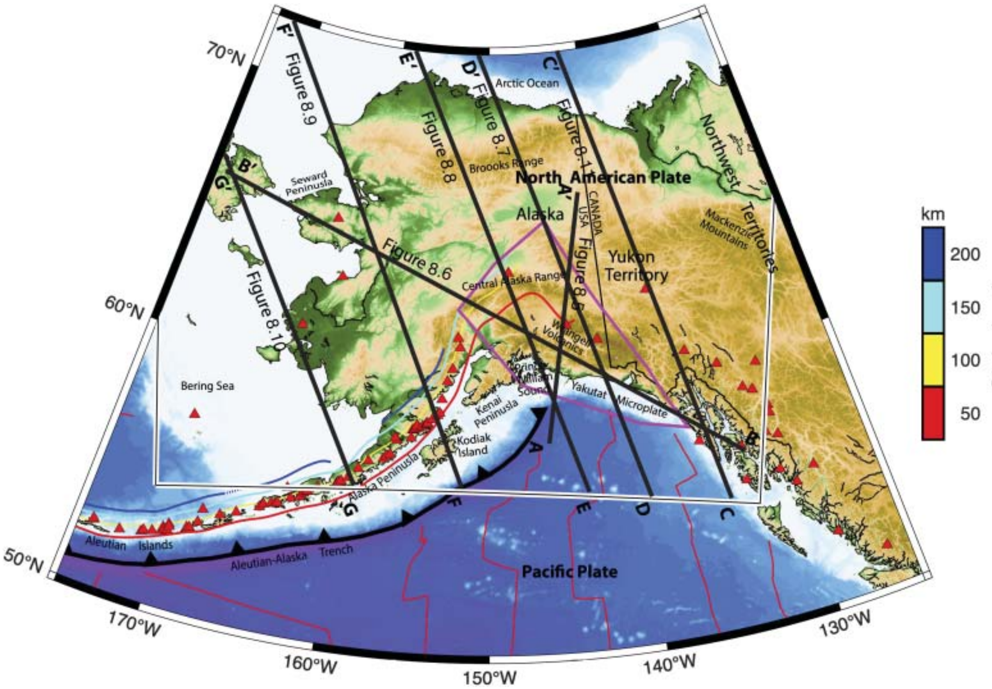

Figure 8.4 Map showing locations of cross-sections AA'–GG'. Figure numbers corresponding to the section lines are also shown. The sections all terminate at the vote map field boundary illustrated as a black line with a white outline. The base map is the same as that in Figure 8.1 but with fewer map layers included.

zone depths and below. It is also truncated to the east very close to the position predicted in the kinematic model of G. L. Pavlis et al. (2019) for the edge of the Yakutat microplate.

8.4.2. Kodiak–Prince William Sound Region

The slab geometry in the Kodiak–Prince William region is shown sliced parallel to plate motion in cross-sections EE' (Figure 8.8) and FF' (Figure 8.9). The eastern side of this region is the flat slab area. Section BB' (Figure 8.6) is a complementary view oriented approximately in the downdip direction in the curved section where the flat slab connects to steeper dips further west. It is noteworthy that the slab geometry inferred from the vote map results (Figures 8.8 and 8.9) is consistent with the surface defined by Slab1.0/2.0 (Hayes et al., 2018, 2012). That is, from east to west, the slab dip defined by Slab1.0/2.0 steadily increases to a more standard slab geometry such as that seen in Figure 8.9.

We assert that the body-wave models are convergent in showing three features of the geometry of the slab in this region that was not known previously:

1. Downstream from the Slab1.0/2.0 surface the anomaly steepens everywhere to be vertical to overturned at the top of the transition zone.
2. The anomalies thicken to widths of 200–400 km at the top of the transition zone. The geometry is suggestive of accumulation of slab material. It is not clear, however, if the model resolutions are sufficient to know if that geometry is real.
3. Within the transition zone the anomaly becomes more diffuse but the models are convergent in showing the anomaly bends to form a south-dipping structure. The structure becomes increasingly diffuse but appears to connect to a similar, south-dipping trend at the maximum depth of 800 km of the vote map volume. That structure, however, seems unlikely to be an artifact because it is nearly universally imaged in the global tomography model vote map results of Shephard et al. (2017).

The geometry of the slab in the region of the Yakutat slab tear may be more complex than appreciated by authors of the individual models we utilized. Figure 8.6 provides a complementary section through this area to Figure 8.8 and horizontal slicing in Figure 8.3. The data suggest that the slab may be folded under the flat slab to have a reversed, southeast-oriented dip above the transition zone. At the eastern edge, there is a more ambiguous (i.e., lower vote count) possible connection to the Yakutat slab that appears to be truncated at a depth of 250–300 km. If this geometry is real, how it could have developed is a subject we return to in the

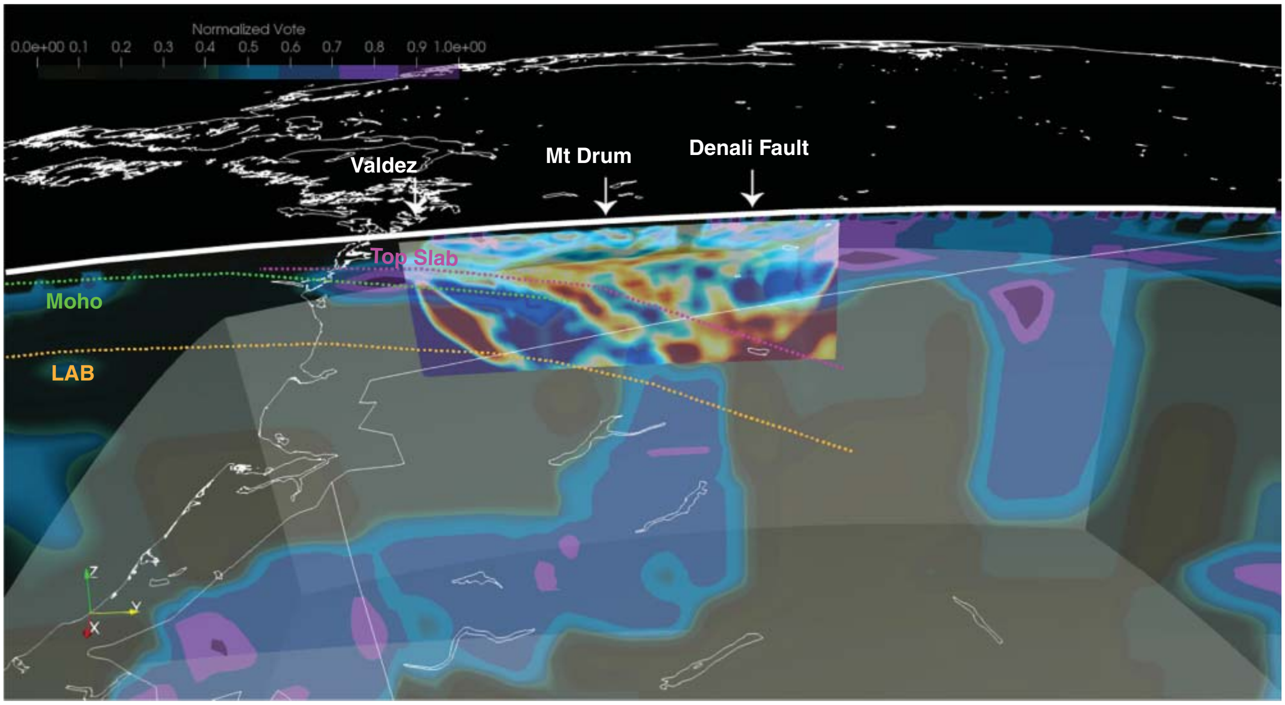

Figure 8.5 Cross-section AA' in the Yakutat–Wrangell region slicing through all image volumes and centered on the wavefield image section from Mann et al. (2022). View is from above and looking southwest normal to the line of the section. The Mann et al. (2022) section is illustrated in true position colored by velocity perturbation with the color bar shown and drawn translucent. We show the vote map section behind the Mann et al. (2022) with the color scale shown in the upper left part of the figure. We draw the intersection of the cross-section plane and crust–mantle boundary (Moho) surface from G. L. Pavlis et al. (2019) in green. Similarly, we draw intersections from G. L. Pavlis et al. (2019) top of slab surface in magenta and lithosphere–asthenosphere boundary (LAB) surface in orange. The background figure shows a translucent, spherical shell surface at a depth of 410 km. That surface serves as a depth reference for the top of the transition zone. The location of this cross-section is illustrated in Figure 8.4. The white line at the top of the section shows Earth's surface and has additional geographic reference tags. A layered version of this figure can be viewed on the companion website with an html tag defined by the figure number. The layered version differs and contains slices through all the models included in this study. Use the layered file to compare the vote map section to other imaging data.

Discussion section, but the geometry is readily seen in Figures 8.6–8.8 and the supplement animations on the companion website.

8.4.3. Aleutian–Alaska Peninsula Region

The slab geometry in the Aleutian–Alaska Peninsula region is shown in cross-section GG' (Figure 8.10). The enhanced coverage of the mantle provided by EarthScope data is limited to a short distance from the coastline. Consequently the models we examined all rapidly lose resolution under the Bering Sea. Figure 8.10 shows two patterns we suggest are reasonably clear:

1. The structure above the transition zone is similar to that we see in the cross-section through Kodiak (Figure 8.10). That is, the slab geometry seen in the vote map slice follows Slab1.0 closely, but downstream from the deepest depth defined in Slab1.0 the dip of the high-velocity feature increases to be very steep to the top of the transition zone.
2. The vote map suggests the slab flattens to become horizontal within the transition zone. That structure, however, is defined only by MIT15 (Burdick et al., 2017) or one of the five models used. That geometry is noteworthy, however, because the global model synthesis by Shephard et al. (2017), which is uses the same concepts as our vote map, indicates global models are similarly convergent in defining this structure.

8.4.4. Yukon Region

The slab geometry in the Yukon region is shown in cross-section CC' (Figure 8.11), and in the horizontal slice maps of Figure 8.3. This area has the highest model coverage with a maximum vote count of five, but also has the same caveat as the western region; the image

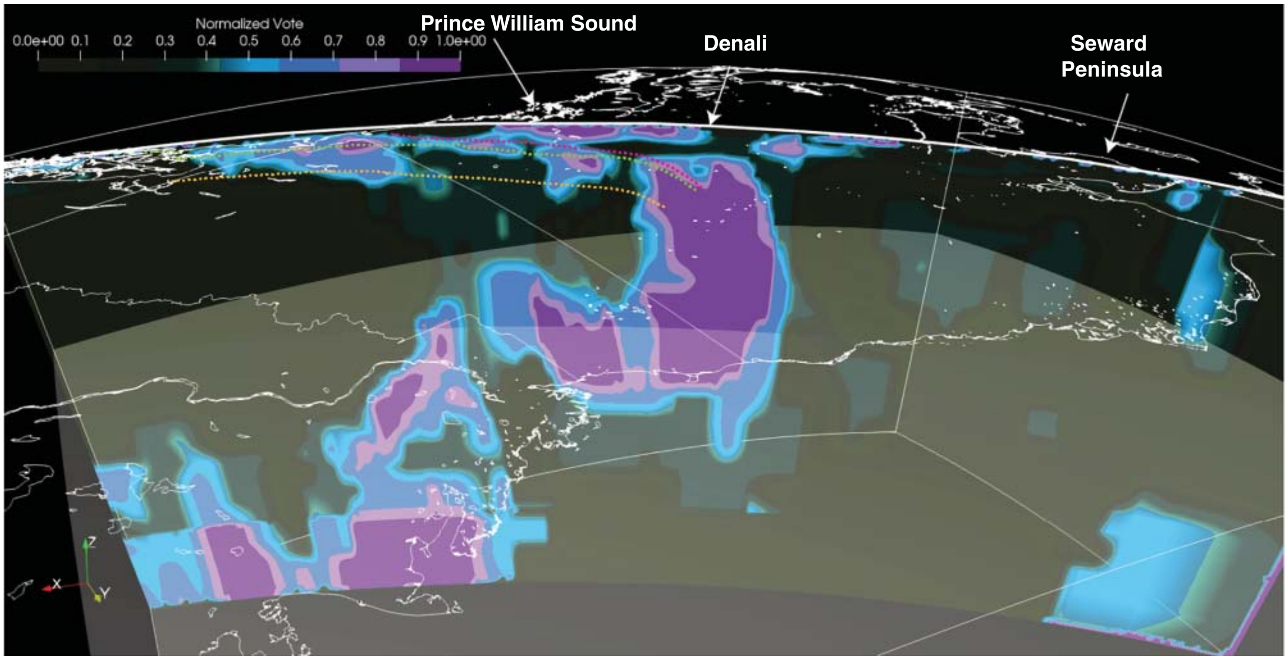

Figure 8.6 Cross-section BB' through vote map image volume. The location of this section is illustrated in map view in Figure 8.4. This section is oriented diagonally across the entire study area and can be thought of as dip section for the western edge of flat slab. View is to the south–southwest (northwest is on image right). See the caption of Figure 8.5 for a description of overlays. A layered version of this figure can be viewed on the companion website with an html tag defined by the figure number. The layered version differs and contains slices through all the models included in this study. Use the layered file to compare the vote map section to other imaging data.

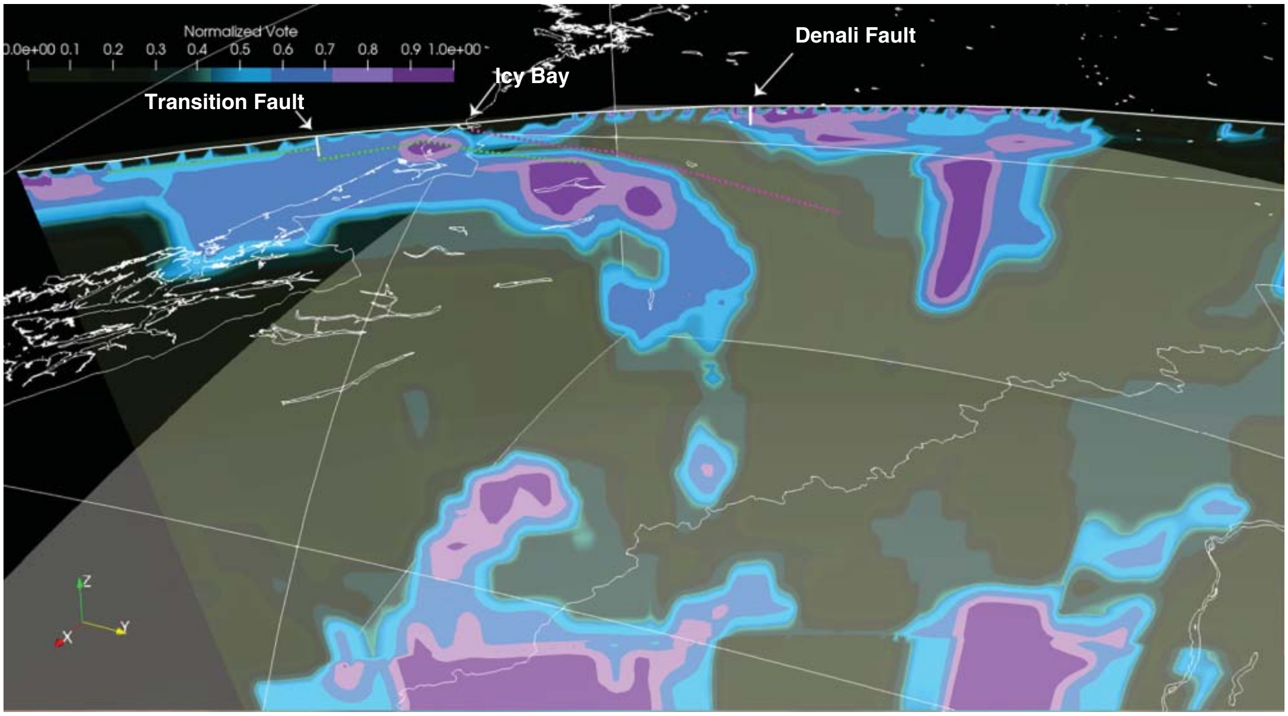

Figure 8.7 Cross-section DD' through vote map image volume. This section passes through the Yakutat–Wrangell region oriented approximately parallel to plate motion and intersecting the coastline near Icy Bay. See Figure 8.4 for a map projection of the section location and the caption of Figure 8.5 for a description of overlays. A layered version of this figure can be viewed on the companion website with an html tag defined by the figure number. The layered version differs and contains slices through all the models included in this study. Use the layered file to compare the vote map section to other imaging data.

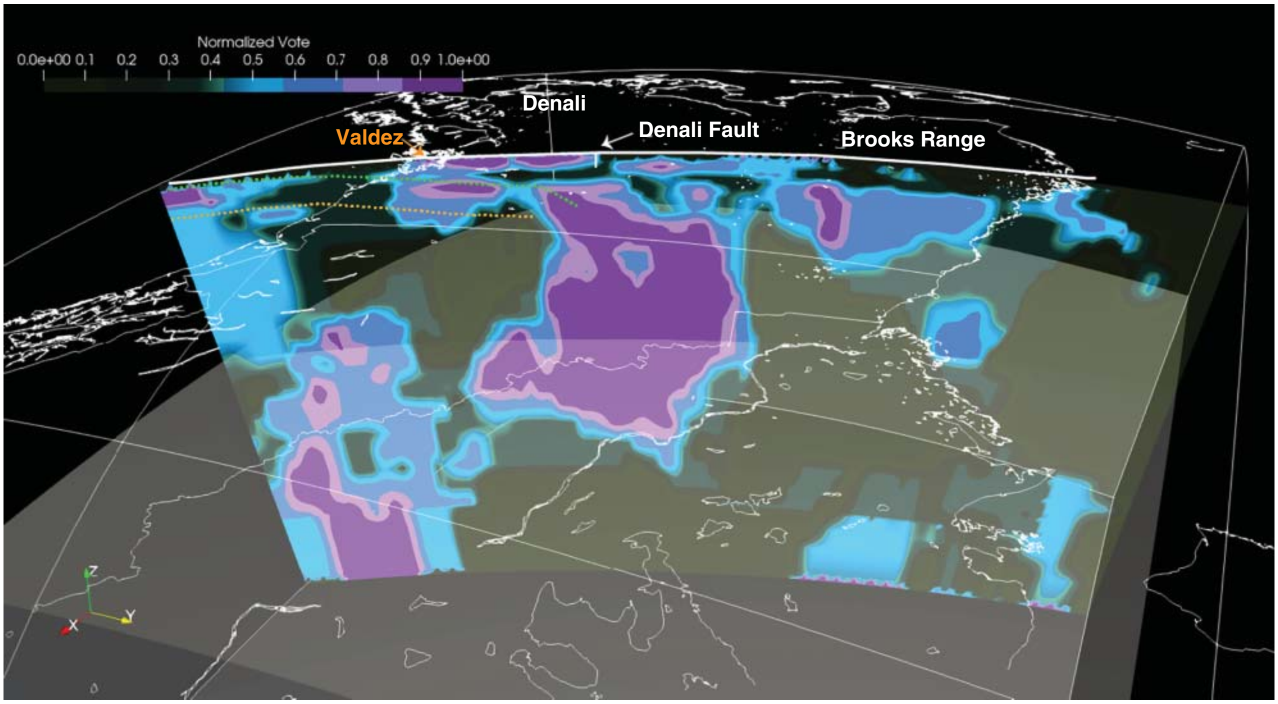

Figure 8.8 Cross-section EE' of vote map data through the center of the flat slab area. This section is oriented approximately parallel to Pacific–North American plate motion passing through the eastern edge of the Kodiak–Prince William Sound near Valdez, Alaska. See Figure 8.4 for a map projection of the section location and the caption of Figure 8.5 for a description of overlays. A layered version of this figure can be viewed on the companion website with an html tag defined by the figure number. The layered version differs and contains slices through all the models included in this study. Use the layered file to compare the vote map section to other imaging data.

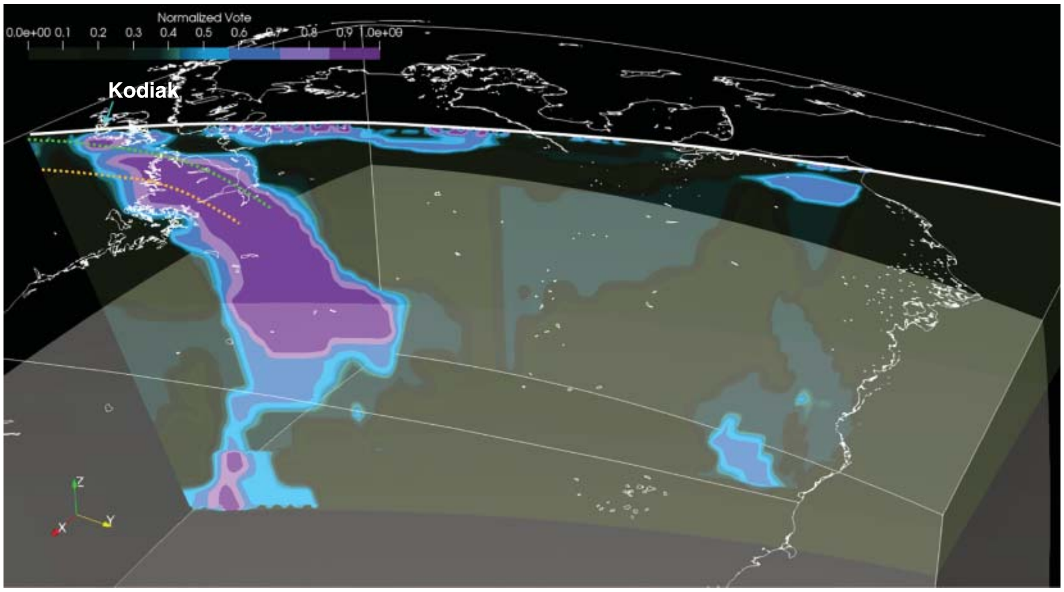

Figure 8.9 Cross-section FF' of vote map data within Alaska but west of the flat slab area. This section oriented approximately parallel to Pacific–North American plate motion and passing through Kodiak, Alaska. See Figure 8.4 for a map projection of the section location and the caption of Figure 8.5 for a description of overlays. A layered version of this figure can be viewed on the companion website with an html tag defined by the figure number. The layered version differs and contains slices through all the models included in this study. Use the layered file to compare the vote map section to other imaging data.

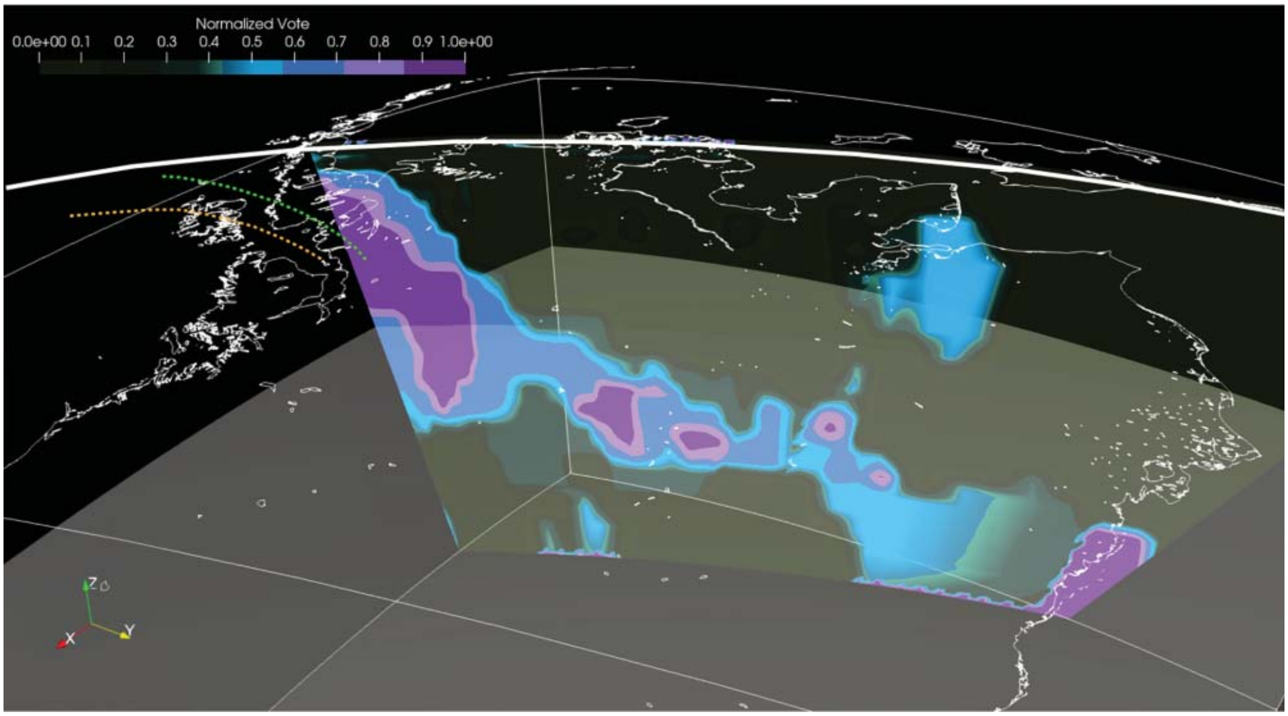

Figure 8.10 Cross-section GG' through vote map image of Aleutian slab geometry under the eastern Bering Sea. This section is oriented approximately parallel to Pacific–North American plate motion and passes near the west coast of Alaska. Most of the section is in the eastern Bering Sea and at the north end passes through eastern Siberia. See Figure 8.4 for a map projection of the section location and the caption of Figure 8.5 for a description of overlays. A layered version of this figure can be viewed on the companion website with an html tag defined by the figure number. The layered version differs and contains slices through all the models included in this study. Use the layered file to compare the vote map section to other imaging data.

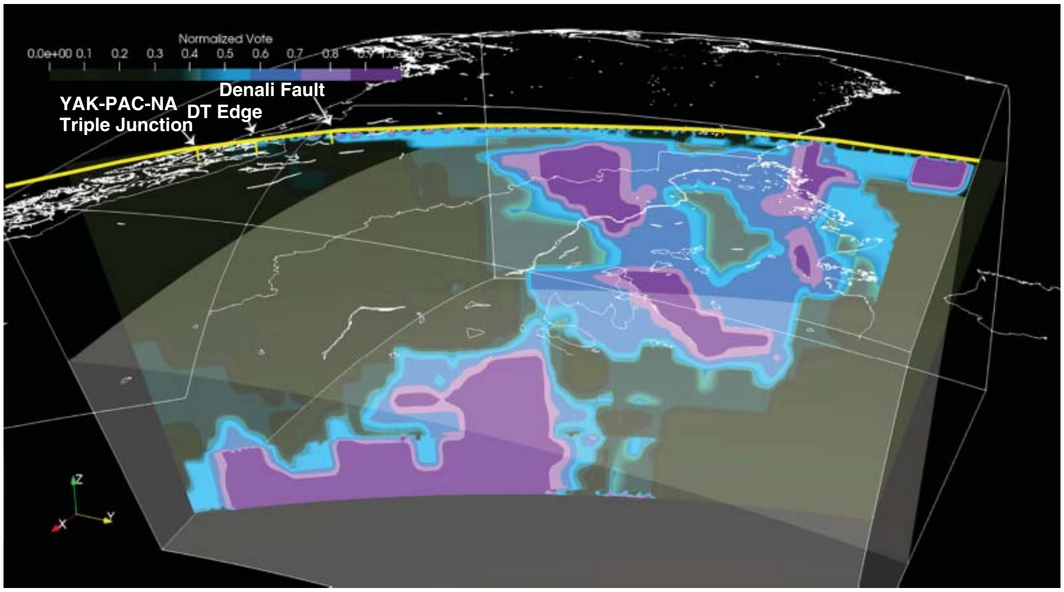

Figure 8.11 Cross-section CC' through vote map image in Yukon region. This section is oriented approximately parallel to Pacific–North American plate motion passing through a point near the international border in the northeast corner of Alaska and the Yakutat–Pacific–North American triple junction. See Figure 8.4 for a map projection of the section location and the caption of Figure 8.5 for a description of overlays. A deviation in this figure is that Earth's surface is drawn in yellow to prevent interference with the irregular (white) coastline in the southern part of the section. A layered version of this figure can be viewed on the companion website with an html tag defined by the figure number. The layered version differs and contains slices through all the models included in this study. Use the layered file to compare the vote map section to other imaging data.

volumes are subject to some edge artifacts. Nonetheless, the basic geometry is defined consistently by all five models we used.

We observe:

1. At shallow to mid-upper-mantle depths, high-velocity anomalies are observed consistently in all models, spanning from the Mackenzie Craton (the Mackenzie platform and Yukon Stable Block) southeast to the Tintina Fault. This is in agreement with the zone of high-velocity material observed in a range of studies, including Esteve et al. (2021) as well as in our companion lithosphere synthesis paper (Yang et al., this monograph) that used a different suite of inversion results.
2. Above the transition zone, the anomaly is unambiguously separated from the high-velocity anomalies we interpret as slab in Alaska. This can be seen most clearly in slices at 300 and 400 km depths in Figure 8.3. Furthermore, this anomaly is laterally offset from the high-velocity cratonic lithosphere underlying the Mackenzie Craton (e.g., Figures 8.5 and 8.7)
3. Figure 8.11, the constant depth slices in Figure 8.3, and the animations on the companion website show the anomaly is steeply dipping, but in the opposite polarity from the modern subduction system. That is to say the high-velocity feature that reaches the transition zone dips to the southwest.
4. The anomaly connects with high-velocity anomalies in the transition zone and lower mantle to form a continuous band with a northeast/southwest strike (500 km slice of Figure 8.3). That structure forms a striking contiguous band in the 800 km depth section of Figure 8.3 that is an arc shape congruent with the current trench but offset to the south by ~ 1000 km from the northern edge of the slab today.

8.5. DISCUSSION

8.5.1. New Constraints on Subduction Geometry

It is important to summarize what we think the EarthScope results have revealed or clarified about the geometry of the subduction system that any interpretation needs to explain.

1. The idea of a slab discontinuity in the Pacific Plate associated with the subduction of the Yakutat microplate has been suggested for some time. That interpretation, however, was based largely on sparse, intermediate-depth seismicity, which made the hypothesis questionable. Zhao et al. (1995) recognized connecting the Wrangell slab to the Pacific–Yakutat slab was not well constrained and included dashed lines in their slab contours in that region, and Fuis et al. (2008) suggested a tear in this region. The integrative study of Jadamec and Billen (2010, 2012) found that a slab geometry with a variable depth extent, including a shorter (~100 km) depth slab below the Wrangell volcanics, was a better to fit to observations. Bauer et al. (2014) argued there was no direct evidence for a tear using S to P imaging results from older, sparser data. It is now clear that Bauer et al.'s interpretation was wrong because that extrapolation was biased by limited coverage. The models examined here and the receiver function imaging of Mann et al. (2022) all provide strong evidence for the existence of a slab discontinuity and place the tear in a similar region to that proposed by Fuis et al. (2008). The line of the slab discontinuity, or tear, closely corresponds to a plate kinematic flow line with an origin at the western limit of the outcrop of Yakutat rocks near Cordova, Alaska (see Figure 4 of G. L. Pavlis et al., 2019). It is noteworthy that Figure 4 from their paper also shows that the rate of intermediate-depth seismicity is orders of magnitude higher west of the tear. The vote map results in this paper indicate that the discontinuity (torn slab) extends to a depth no greater than 350 km.
2. The geometry of the slab where it is constrained by shallow to intermediate-depth earthquakes has been well known since the publication of the local earthquake tomography model by Eberhart-Phillips et al. (2006). Prior to the TA deployment, the deeper geometry of the slab, however, was poorly constrained. The only constraints on deeper structure came from global tomography models. We find that downstream from the edge of Slab1.0/2.0, which is mainly constrained by seismicity, the slab dip steepens to be nearly vertical under all of Alaska.
3. A feature of the deeper structure of the slab that was not as clear from individual body-wave results is the geometry of the downgoing Pacific slab from the top of the transition zone (410 discontinuity) to the maximum depth range of all the models (800 km). The models are convergent in showing the slab is offset southward into what can be described as a recumbent fold with a nose near the top of the transition zone. The fold structure extends from the Yakutat slab tear at the eastern edge of the flat slab to flow lines passing near the Alaskan west coast. Our vote map data suggest that under the Bering Sea the slab reverses into a flat-lying, high-velocity anomaly within the transition zone. We caution, however, that the structure in that region has a poor resolution for all but the MIT model of Burdick et al. (2017), which is a combined global and local model. The global tomography synthesis with a comparable vote map method of Shephard et al. (2017), however, suggests

that this is the likely geometry in that region of the transition zone.

4. A new feature completely unknown prior to the EarthScope TA deployment is a near vertical, high-velocity anomaly located approximately under the Yukon River in east-central Alaska. We note three important geometric features of this anomaly. First, it is a contiguous extension of the near vertical, high-velocity anomaly seen by all body-wave models under the northern edge of the Slab1.0/2.0 surface. Second, the eastward limit of the anomaly corresponds to the slab edge predicted from rigid plate kinematics by G. L. Pavlis et al. (2019). This relationship suggests strongly that it may be related to the predominate strike-slip motion of Pacific–North America that has characterized plate motions for the last 40 Ma. Finally, within the resolution of the data, it is a reasonable conjecture that the Yakutat slab tear can be characterized as a flap that if unfolded upward would be contiguous with the Yukon River anomaly. We note this same feature was interpreted by Esteve et al. (2020) as a piece of craton 'chiseled' from the Mackenzie craton by the Tintina Fault. The Yukon River anomaly was at the edge of their study area and, they were unaware of the connection of this feature with the slab to the west. That alternative interpretation is thus questionable.
5. The models are convergent in showing a gap between the eastern limit of the Yukon River anomaly and another high-velocity anomaly observed in all models under the Yukon Territory. Fuston and Wu (2020) called this anomaly the Yukon slab. They argued that this feature is linked to the Kula–Farallon subduction system. The fact that this feature is located well east of the edge predicted by rigid plate kinematics shown in Figure 8.3 is additional support for Fuston and Wu's model that links this slab to Kula–Farallon subduction. A new feature suggested from this synthesis is that the Yukon anomaly seems to be connected to the lower-mantle anomaly south of the modern trench. That link provides additional evidence that the lower-mantle anomaly might be a record of Kula–Farallon subduction.

We note that additional confirmation of the validity of our results can be seen in recent work by Boyce et al. (2023). They used the same methods as MIT15 but added additional data from Canada. That work was not available to use when we did the vote map analysis but is consistent with all of the above.

8.5.2. Folding of the Pacific Slab

Global observations on the location and orientation of subducted oceanic lithosphere indicate that modern slabs display a range in geometries at depth, including varying slab orientations at the mantle transition zone where there is an increase in mantle viscosity from the upper to the lower mantle (Fuston & Wu, 2020; Goes et al., 2017; Gudmundsson & Sambridge, 1998; Hayes et al., 2018; Jadamec et al., 2018b; Jarrard, 1986; Lallemand et al., 2005; Li et al., 2008). Here, we consider the EarthScope results in the context of a possible large-scale fold in the Pacific slab, geodynamic mechanisms for large-scale slab distortion, and implications for the flat slab at shallower depths.

Seismic Constraints on a Large-Scale Folding of the Pacific Slab at the Transition Zone

The EarthScope results provide evidence that the Pacific slab in the Kodiak–Prince William Sound region is curved at the mantle transition zone, with the apex of the curve oriented convex to the northwest. Here, the lowermost segment of the best imaged part of slab is bent back toward the trench to form a lithospheric scale, northwest-closing recumbent fold, with the nose of the fold at depth around 350 km. The structure appears to continue through the transition zone to the maximum common depth of the models we used at 800 km. We reiterate that the feature revealed by the EarthScope results directly connects with a structure in the lower mantle revealed by similar vote map methods applied to global tomography models by Shephard et al. (2017). That geometry is illustrated in Figure 8.15 in the 40 Ma frame. Comparison of those two figures shows that the lower-mantle anomaly at 1000 km is consistent with the anomaly at 700 km illustrated in Figure 8.12.

The southward bending of the plate at depths below 300 km is also supported independently by the receiver function imaging of the transition zone by Dahm et al. (2017) and van Siphout et al. (2019). Both papers used the CCP method and utilized available 3-D models to build more accurate maps of the depth to the 410 and 660 discontinuities. Both papers discuss at length the limitations of existing models in fully capturing the large anomalies created by the slab in this region. Their results are convergent, however, in showing an elevation of the 410 discontinuity where the tomography models show positive velocity perturbations that we are interpreting as the subducting slab position. In addition, both papers note that topography of the 660 km discontinuity is muted, compared to that seen on the 410. Dahm et al. (2017) suggest "cold slab segments are mostly in the upper mantle transition zone (MTZ) and at deeper depths it 'is probably broken into fragments.'" Similarly, van Siphout et al. (2019) conclude 'the slab must end within the MTZ.' Our results and the related global tomography synthesis of Shephard et al. (2017) suggest that one needs to explain the connection of the well-imaged upper-mantle

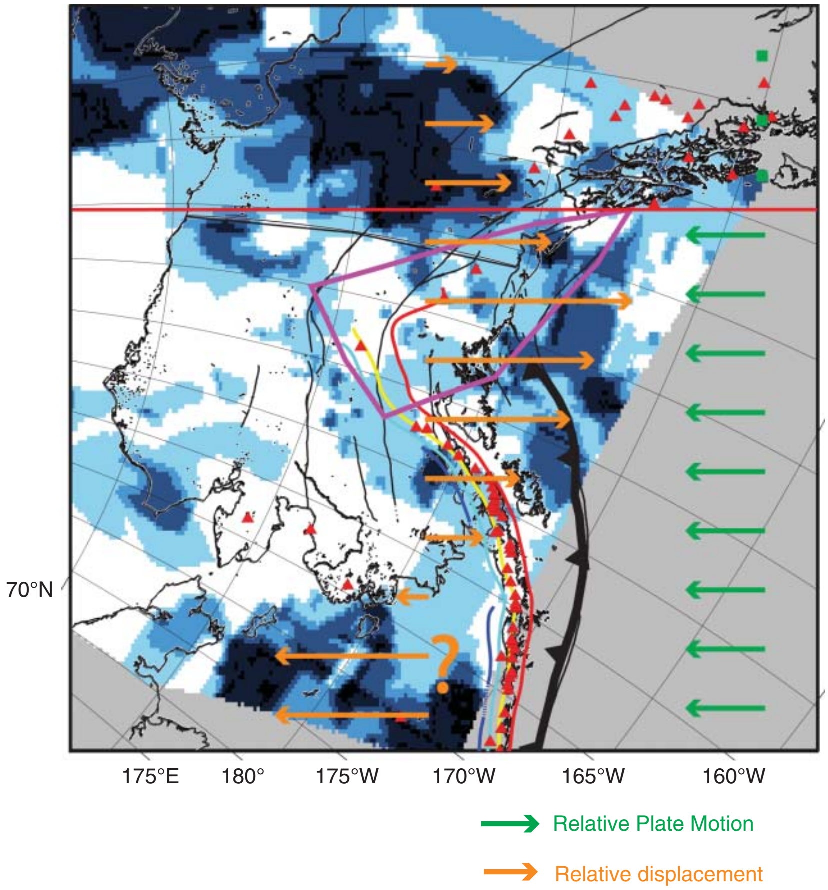

Figure 8.12 Interpretation of relative displacement between the shallow portion of the slab (at 100 km) and base of the imaging volume (at 700 km). Base map: 700 km depth slice. Oblique Mercator projection with a pole at the modern pole of rotation between the Pacific and North American plates. Thin gray curves: normal constant latitude and longitude lines with labels at the plot boundaries. Heavy, red, horizontal line: constant latitude line in this projection that defines pure strike-slip motion with modern plate motion passing through the Yakutat–Pacific–North America triple junction. The green squares and vectors emphasize that this is not a normal map projection. Above the red line the squares are used to imply zero relative motion. Below the red lines the vectors are constant because the projection is constant angle around the pole of rotation. Orange arrows: interpreted displacement of slab current slab location at 700 km depth with respect to current slab location at 100 km depth. The companion website has a layered version of this same figure that shows the slices at both 100 and 700 km depths illustrating the offset between the two horizons. Color scale for the vote map section is the same as Figure 8.3. Question mark by the orange arrows on the western side of the study area (bottom of the figure) indicates transition zone structure that is not well resolved. Other features in base map are the same as described in the caption of Figure 8.1.

structure to the lower-mantle structure seen in deeper slices of Figure 8.3 and illustrated in the 40 Ma panel of Figure 8.15.

We suggest that the lower-mantle structure is the remnant of earlier subduction, and the muted structures in the transition zone imaged from the EarthScope TA data mark the descent path of slab material through the transition zone. van Siphout et al. (2019) suggest an alternative hypothesis that the slab is truncated in the transition zone. We assert that hypothesis is unlikely to be true as it is inconsistent with the fact that over 2000 km of lithosphere has been consumed in this subduction zone with a nearly constant trajectory and rate for the past 40 Myr. For a slab that long to be terminated in the transition zone, it would need to be shortened by a factor of four or more along the convergence direction. That is not inconceivable but cannot be answered without additional work. Hence, we suggest the more likely scenario is that the slab is continuous through the transition zone, but as Dahm et al. (2017) suggest have disaggregated as the material descended through the transition zone. Our results suggest that the high-velocity anomaly we interpret as slab thickens at the top of the transition zone, which could be explained by compressional strain and/or folding of the slab in the 300–400 km depth range. Some or all of the slab material may then penetrate the transition zone and connect to the lower mantle anomaly as suggested in Figure 8.12. It is questionable if our results or any of the individual tomography models are reliable enough to address this issue. In principle, the methods of Wu et al. (2016) could be used to estimate the amount of possible shortening of the slab above the transition zone to test a hypothesis that all of the slab is piled up near the top of the transition zone.

The EarthScope results also suggest that this large-scale slab structure beneath the Kodiak–Prince William region may straighten out westward so that the slab impinges into the transition zone in a more vertical fashion. To the west in the Aleutian–Alaska Peninsula section, the EarthScope results suggest that the Pacific slab then rests flat on the transition zone forming a secondary fold along a vertical shear zone parallel to plate motion.

Quantifying Fold Distortion and Discussion of Mechanisms

We can estimate the distortion of the folded lithosphere by a lithosphere-scale version using a geologic marker. The marker in this case is the interpreted top of the subducting slab. Figure 8.12 illustrates how the observed position of high wavespeed anomalies is displaced between the base of the lithosphere and lower mantle. The orange arrows were produced by drawing lines on the figure parallel to Pacific–North American plate motion that connected the anomaly at 100 and 700 km depths (These can been seen as separate layers in a layered version of this figure on the companion website). We remind the reader that with the oblique Mercator projection used in that figure, the rigid plate motion of the Pacific Plate relative to North America is defined by constant angular velocity vectors that become nonzero west of strike slip boundary along the west coast of Canada (bottom of the figure). The constant length, green arrows in Figure 8.12 emphasize that geometry. That also means the orange vectors illustrating the folding of the slab do not have a fixed distance scale but are also scaled by angular velocity.

We then aligned the tails of all the orange arrows to compare the displacement in the different regions of the study area and applied some artistic license to smooth the vectors. We stress this figure is not just a sketch, although it is not completely objective either. It is an interpretation that makes some key assumptions. First, it assumes the high velocity bodies we are using for this interpretation are real and define a continuous structure. How reliable that assumption is depends on location and depth. That assumption is probably pretty solid throughout all of central Alaska but is tenuous in the eastern Yukon and Bering Sea. All the models also suffer from a progressive loss of resolution with depth so the position of the arrows defined by the 700 km slice is less reliable than that derived from the 100 km depth slice. Second, we assume that the deformation process creating this feature will make the deformed slab smooth at the scale we can resolve it with these models. For that reason, the original measured vectors were stretched and shortened to produce the smooth profile seen in the figures.

Nonetheless, the relative displacement field in Figure 8.12 shows that, in the Kodiak–Prince William Sound region, the slab at 700 km depth is several hundred kilometers to the south of the location of the slab at 100 km, suggesting the recumbent fold in the slab with the apex to the northwest. Conducting a similar examination of the proxy displacement vectors in the Aleutian–Alaska Peninsula region of the study area shows that the direction of displacement reverses, with the arrows now pointing to the north. This indicates that the slab at 700 km is north of the position of the slab at 100 km, suggesting that in the Aleutian–Alaska Peninsula region the slab is laying flat in the mantle transition zone.

Global observations and geodynamic modeling suggest there may be a correlation between the nature of the interaction of a slab with the transition zone and whether the subduction zone trench is in advance or retreat. Slabs that fold forward tend to be correlated with advancing trenches, and slabs that lay flat on the transition zone tend to be correlated with trench retreat and slab rollback (e.g., Bellahsen et al., 2005; Sharples et al., 2014). In the Aleutian–Alaska subduction zone, there is a transition from trench retreat in the Aleutian subduction segment to advance and/or trench stagnation in the Alaska subduction zone segment (Schellart et al., 2008). Thus, there appears to be a correlation with the slab geometries we are observing, in that the recumbent slab in the Kodiak–Prince William Sound region corresponds to a trench that is either stagnant or advancing, and the slab laying flat on the mantle in the Aleutian–Alaska section correlates with trench retreat in the Aleutians. We note that this is just a first-order observation and does not attempt to explain a mechanism.

Studies of the driving and resisting forces of subduction indicate there are multiple tectonic factors that can influence the dip of a slab, both at shallow and deeper depths (Billen, 2008; Gerya, 2011; Goes et al., 2017; Lallemand et al., 2005; van Hunen et al., 2004). For example, 2-D and 3-D geodynamic models of subduction have shown that slab dip can vary as a function of localized decreases in asthenospheric viscosity due to mantle rheology (Billen & Hirth, 2007); variations in upper plate thickness, strength, and density (Manea et al., 2012; Sharples et al., 2014); the subduction of ridges and/or oceanic plateaus (Arrial & Billen, 2013; Martinod et al., 2005; Mason et al., 2010); variations in the along strike age of the oceanic lithosphere

(Capitanio & Faccenda, 2012; Morra et al., 2006); variations in the along strike length of the incoming plate (Shellart et al., 2007), motion of the overriding plate (Sobolev & Bsbeyko, 2005), and mantle viscosity jumps at the transition zone as well as phase changes within the slab at the transition zone (Goes et al., 2017; Pysklywec & Ishii, 2005). For the case of Alaska, many of the physical factors that could lead to an advancing/stagnant trench and/or a folded slab recumbent slab to the north are present (Arrial & Billen, 2013; Finzel et al., 2011; Haynie & Jadamec, 2017; Koons et al., 2010; Morra et al., 2006; G. L. Pavlis et al., 2019), so our observations are not unexpected. On the other hand, the observations alone cannot distinguish between the competing mechanisms.

Slab dynamics are likely complicated in the Yakutat–Wrangell area and Yukon area, where the mantle flow field in the corner almost certainly has 3-D elements that are not captured in the simple graphic of Figure 8.12. High-resolution geodynamic models of 3-D subduction and mantle flow in Alaska predict counterclockwise toroidal flow and slab edge upwelling in this region (Jadamec & Billen, 2010, 2012). In addition, seismic anisotropy results (Guo et al., 2019; Hanna & Long, 2012; McPherson et al., 2020) suggest that toroidal flow is, in fact, present around the eastern edge of the slab in the vicinity of the Yakutat slab discontinuity.

The existence of the 'Yukon slab' (Fuston & Wu, 2020) illustrated in Figure 8.11 likely further complicates slab dynamics. Fuston and Wu (2020) argue that anomaly is linked to Kula subduction. Our results support Fuston and Wu's conclusion but add the possible connection of that feature with the high-velocity, lower mantle anomaly imaged in global tomography. That complicates this problem because a comprehensive solution will require a 4-D geodynamic model to evaluate what features in these results are plausible with realistic constraints on mantle rheology.

Implications for the Origin of the Flat Slab

For the past 20 years the idea that the flat slab in Alaska was created by the subduction of anomalous crust linked to the Yakutat microplate has become nearly axiomatic (e.g. Finzel et al., 2011). The new data from EarthScope as well as independent models of flat slab subduction suggest that the subduction of anomalous crust may not be the only process responsible for creating the flat slab (e.g. Sobolev & Babeyko, 2005; Morra et al., 2006; Manea et al., 2012; Sharples et al., 2014). For the Alaska case, multiple tectonic factors in the Alaska subduction zone could lead to a flat slab beneath Prince William Sound, such as the eastward younging in the age of the Pacific Plate, trench advance, overriding plate motion, and interaction with the transition zone, in addition to the subduction of an oceanic plateau. In addition, as Figure 8.15 illustrates, Pacific Plate motion shifted westward relative to North America at around 33.5 Ma. Provided the subducting lithosphere has sufficient rigidity to remain intact, the westward pull that motion requires may induce upwelling on the eastern edge of the subducting plate. In addition, to initiating Wrangell volcanism as advocated by Trop et al. (2021), upwelling may have also set up pressure gradients near the eastern edge of the slab that could be a factor in the initiation of the flat slat as early as 30 Ma. However, additional geodynamic modeling would be required to test that hypothesis. The overall 3-D perspective (see animations and the 3-D PDF on the companion website) suggests that the lithosphere in the center of Alaska (the flat slab) is located above remnants of the deeper slab in the transition zone that in turn may link with (older) slab remnants in the lower mantle south of the modern trench. If that hypothetical geometry is real, then the geodynamic process(es) that created that geometry cannot be sorted out without physics-based simulations and/or more focused seismic imaging on key components of the system.

8.5.3. Constraints on a Yakutat Tear

Timing Constraints

Given the strong new evidence for the existence of a tear in the plate linked to the Yakutat microplate, an open question that has not been carefully addressed is when that tear developed? Figure 8.13 shows that plate tectonic kinematics require that the Yakutat slab tear could not have initiated earlier than around 10 Ma. We suggest that a better estimate is that the tear began between 7 and 9 Ma. That estimate hinges on an interpretation based on Figure 8.7. For that estimate we have to assume that to first order the tear in the plate downstream from the Yakutat microplate can be thought of as a flap folded downward. The reader can verify this themselves by looking closely at the true geometry section in Figure 8.7. The bottom of the torn section when rotated upward intersects approximately the southern edge of the Yukon River anomaly. If we further assume the Yakutat slab has not been shortened significantly by internal, compressional strain, then the northern edge of the polygon outline (left of the polygon in the figure) is approximately a constant time line.

Figure 8.13 shows that the leading edge of what is now the northern edge of the flat slab first crossed the position of the modern coastline at around 20 Ma. The leading edge of what became the tear did not cross that point until around 10 Ma. Our 7–9 Ma suggestion comes from a simple geometric model based on distance and rigid plate motion. We approximate the slab as a dipping plane moving at a constant convergence velocity to estimate the

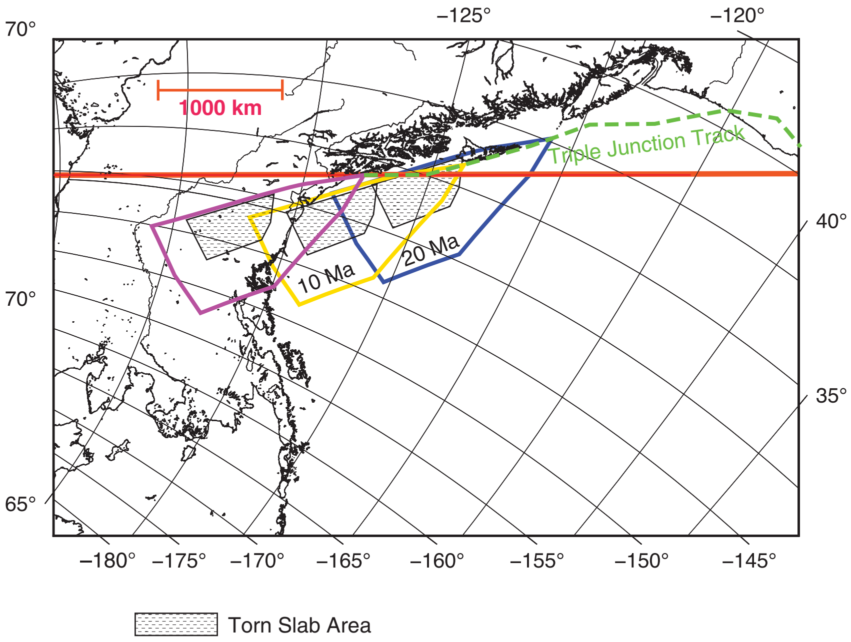

Figure 8.13 Backprojections of Yakutat polygon showing first-order timing constraints on the Yakutat tear. The base map of this figure is the same oblique Mercator projection seen in Figure 8.12. See the caption of that figure for common features. The purple polygon is the outline of Yakutat lithosphere from G. L. Pavlis et al. (2019). The hatched area is our interpretation of the map area of the tear in the slab seen today in eastern Alaska and discussed at length in the text. The yellow polygon is the backprojection of the purple polygon to 10 Ma using the plate model of Doubrovine and Tarduno (2008). The yellow polygon includes a backprojection of the tear region. The blue polygon and enclosed hatched are the comparable projection to 20 Ma. We also illustrate the backprojection of the Yakutat–North America–Pacific triple junction to 45 Ma with the same plate model as a dashed, green curve. The companion website has a layered version of this figure that may help the reader understand this figure by reducing overlaping elements.

time for the base of the tear to reach the current depth of 300–350 km. If θ is the dip angle and v is the local plate convergence rate, then the time, T, for the top of the subducting slab to move from depth z_0 to z is

$$T = \frac{z - z_0}{v \sin \theta} \tag{8.1}$$

Using the modern rate to one significant figure of 50 mm/year, $\theta = 45^\circ$, and $z_0 = 30$ km, we compute times of 7.6 and 9 My for $z = 300$ and 350 km depths, respectively. If we change the average angle to 30° and 60° in combination with the upper and lower bounds on z, we can bound the time between 6 and 13 My. This is an overly simplistic geometric model, and does not include any 3-D thermomechanical analysis, but it is useful because it demonstrates an important inconsistency. The longest reasonable time for initiation of the tear is far less than the oldest volcanics found in the Wrangells of 30 Ma in the most recent work by Trop et al. (2021). We suggest several hypotheses to explain this inconsistency. First, the inferred truncation of the torn slab may not be real. Figure 8.7 hints that the slab may be folded under to the south to connect with lower-mantle structures as we discussed above for the area west of the flat slab. More careful imaging focused on addressing this issue would be required to confirm or deny that hypothesis. Additional hypotheses include slab edge-induced volcanism, initially predicted by high-resolution 3-D modeling of the eastern Alaska slab edge (Jadamec, 2016; Jadamec & Billen, 2010, 2012) as well as other related anomalous volcanism mechanisms (Berkelhammer et al., 2019; Brueseke et al., 2019; Trop et al., 2021). We assume that anomalous edge-related/slab window mechanisms are true in our kinematic model for the past 40 Ma below.

Kula Ridge Slab Gap Hypothesis

Figure 8.14 illustrates a new hypothesis worth considering as a factor in the origin of a Yakutat slab tear and its relation to the Yukon River anomaly. That model is based on two, interwoven concepts. First, we noted above that in the period prior to 40–45 Ma the western margin of the northern Cordillera was the site of subduction of the Kula Plate. The figure shows backprojections of oceanic crust age contours to 40 Ma using stage poles for Pacific–North America motion from Doubrovine

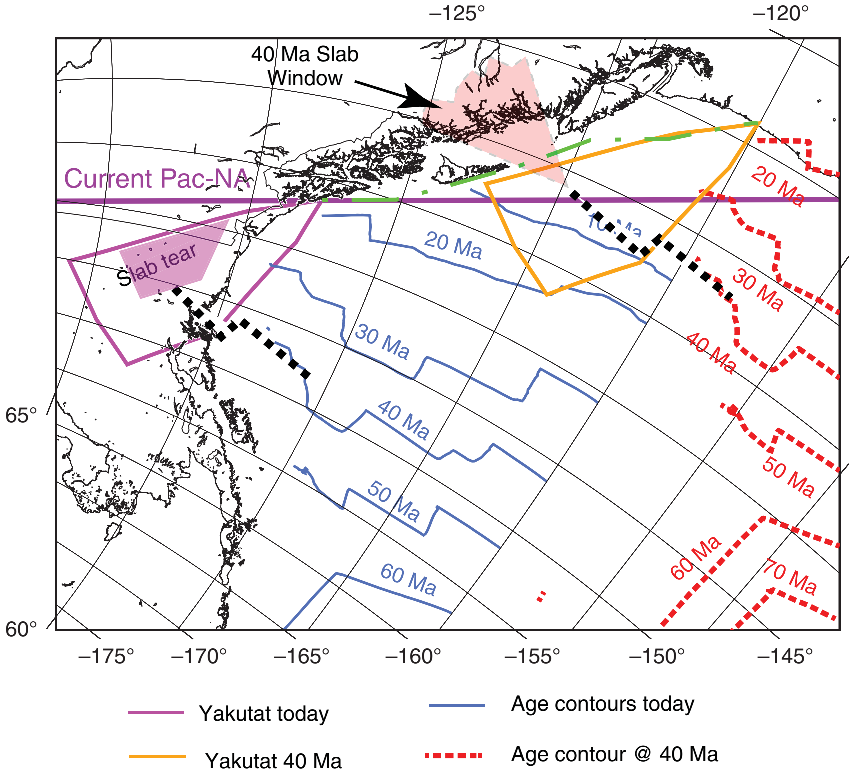

Figure 8.14 Illustration of how a slab window linked to the extinct Kula ridge may be linked to the Yakutat slab tear. Map base is an oblique Mercator projection identical to Figure 8.13. See the caption of that figure for details of the projection. A difference is that the horizontal red line was made purple here to avoid ambiguity with other map elements. The blue lines on the base map show age of the oceanic crust in 10 Ma intervals (Müller et al., 2008) in their modern map position. The red lines are the same data backprojected to 40 Ma using the plate model of Doubrovine and Tarduno (2008). The current position of the Yakutat microplate polygon from G. L. Pavlis et al. (2019) is illustrated in magenta along with our interpreted map area of the Yakutat tear. The projection of that polygon to 40 Ma using the same plate model is illustrated in orange. The heavy, black, dashed curve on the left is our proposed location for the Kula ridge at 40 Ma. The translucent pink fan-shaped area above the curve is the projection of a slab window that would have been required if the Kula ridge were in that position. We show the forward projection of the black, dashed curve to the present to illustrate that it intersects the modern location of the Yakutat slab tear. This figure has a supporting layered graphic on the companion website. A key element of the supplementary figure not possible to illustrate with this simple figure is the position of the Kula ridge at 40 Ma proposed by previous authors. See the companion website to evaluate the reliability of our proposed Kula ridge position in relation to previouly published models.

and Tarduno (2008). A layered version of Figure 8.14 found on the companion website shows the approximate position various authors sketched as the position of the ancestral Kula ridge at 40 Ma. The position we illustrate in Figure 8.14 is within the range suggested by previous authors. The second concept is that of a slab window. Dickinson and Snyder (1979) were the first to introduce the idea of a slab window linked to ridge subduction and the creation of the San Andreas transform. Thorkelson (1996) developed that idea into a comprehensive discussion of the range of kinematic constraints required in the subduction of ridges and creation of slab windows. Thorkelson and colleagues have since written a series of papers exploring how slab windows impacted western Canada during the Kula period (e.g. Madsen et al., 2006). We adapt that idea in Figure 8.14 by noting that the location of the Yakutat slab tear is within the range of previous authors projection of where the Kula ridge was being subducted at the time of the major plate reorganization between 40 and 45 Ma. The basic idea of this model is that the slab window was transported northward along with the Yakutat microplate from 45 Ma forward and formed a zone of weakness that created the Yakutat slab tear when it was subducted. Note that an alternative hypothesis would be that the tear was generated via some 3-D slab detachment process (e.g.

Burkett & Billen, 2010) after initial subduction beneath Alaska. Future time-dependent geodynamic modeling would be required to test which of these hypotheses are feasible.

8.5.4. Kinematic Model

Figure 8.15 illustrates a kinematic model that is consistent with all the data discussed in this chapter. The time snapshots in the figure where chosen to be even numbers that are within time ranges of Pacific–North American stage poles defined in the model of Doubrovine & Tarduno (2008). We describe the history implied by this model going forward from Kula times.

Before 40 Ma. Figure 8.15 does not illustrate history prior to 40 Ma. As noted above, that earlier history is defined by the poorly constrained 'death' of the Kula plate and the major change in relative motion of the Pacific Plate that happened between 50 and 40 Ma. A key point to realize as a starting point for the history, however, is that the prevailing model is that the early Cenozoic history was defined by subduction along the entire west coast of Canada and Alaska. Starting our reconstruction at 40 Ma means we avoid the unresolved issue of the origin of the Yakutat microplate. This study has no new data that can contribute to resolving that issue. The kinematics only suggests that what happened to create the Yakutat microplate is most likely tied up in the complex story of the death of the Kula plate and the related history of the Siletzia terrain as discussed by Wells et al. (2014).

40 Ma. Our first panel in Figure 8.15 is a backprojection to 40 Ma. By that time, Pacific–North America relative motion had resolved to almost the same direction as today but with a different velocity. Furthermore, the fact that the backprojected polygon shown closely matches the coastline in every frame of this reconstruction suggests that the Yakutat microplate has not rotated significantly during its northward transport. That implies there has been little motion on the Transition Fault for the past 40 Ma and whatever process created the offset in the Moho at that Transition Fault (Christeson et al., 2010) happened before 40 Ma.

In the figure, we display the outline of a high-velocity body in the lower mantle seen in the synthesis of global tomography models by Shephard et al. (2017). Because of that location we suggest that the trench at that time may have been south of its current location. We also illustrate a variation of an idea that originated with Plafker and Berg (1994). They hypothesized that the Yakutat microplate began its northward transport around 25 Ma via an eastward jump in the plate boundary to the vicinity of the modern Fairweather Fault. Newer data indicate the volcanic gap ended earlier at around 30 Ma (Trop et al., 2021). Further, the kinematic model illustrated in Figure 8.15 shows there is no clear agent to have induced such a jump at 30 Ma. We suggest one possible solution is the strike slip boundary illustrated with the label 'DRZ?' (Dangerous River Zone) on the right. The term DRZ was coined by Plafker et al. (Plafker, Moore, & Winkler, 1994). Analysis of active source data in STEEP by Worthington et al. (2012) demonstrated that the DRZ was a major crustal boundary with only a thin package of sediment east of the boundary and a wedge of sediment that thickened to the west. Figure 8.15 illustrates that the geometry works for the DRZ to have been the plate boundary in the 40–33.5 Ma stage of the Doubrovine and Tarduno (2008) model. A projection of the known location of the DRZ today parallel to plate motion could explain the volcanic gap with the same logic as that of Plafker and Berg (1994).

33.5–25.7 Ma. Doubrovine and Tarduno's model indicates that the motion of the Pacific during this period shifted slightly eastward with a minor rate increase at 33.5 Ma. Our suggestion for the geometry at 30 Ma is driven by the need to explain the initiation of the Wrangells at 30 Ma. We have utilized the hypothesis of Trop et al. (2021) that the early volcanism in the the Wrangells reflected corner flow. We add the constraint from Finzel et al. (2011) that volcanism ended in the area of the modern flat slab region around 30 Ma. That suggests something dramatic happened on the plate boundary to initiate that transition. If this model is correct, then what agent created this change is not clear. The plate motion change at 33.5 was relatively small.

25.7–6 Ma. Doubrovine and Tarduno's model says that unlike the small change at 33.5 Ma, at 25.7 Ma there was a large westward shift in the motion of the Pacific relative to North America along with a 20% rate increase. That motion continued until 6 Ma with a small change in velocity at 16.7 Ma. Our panels for 20 and 10 Ma illustrate a concept we do not believe has been considered in previous publications on this region. That is, after such a change the eastern edge of the subducting mantle lithosphere would, of necessity, have to undergo extension relative to the motion from 40–25.7 Ma. Did that geometry create an upwelling that drove Wrangell volcanism and migration of the volcanic field since then (Jadamec, 2016; Jadamec & Billen, 2010, 2012; Richter et al., 1990; Trop et al., 2021) and/or the initiation of the flat slab? Figure 8.15 suggests the geometry is right for that hypothesis to be true. Additional physics-based geodynamic modeling is needed, however, to validate or reject that hypothesis.

6 Ma to present. At 6 Ma, the plate motion shifted to a direction nearly identical to what it was in the 33.5–25.7 Ma stage in Doubrovine and Tarduno's model.

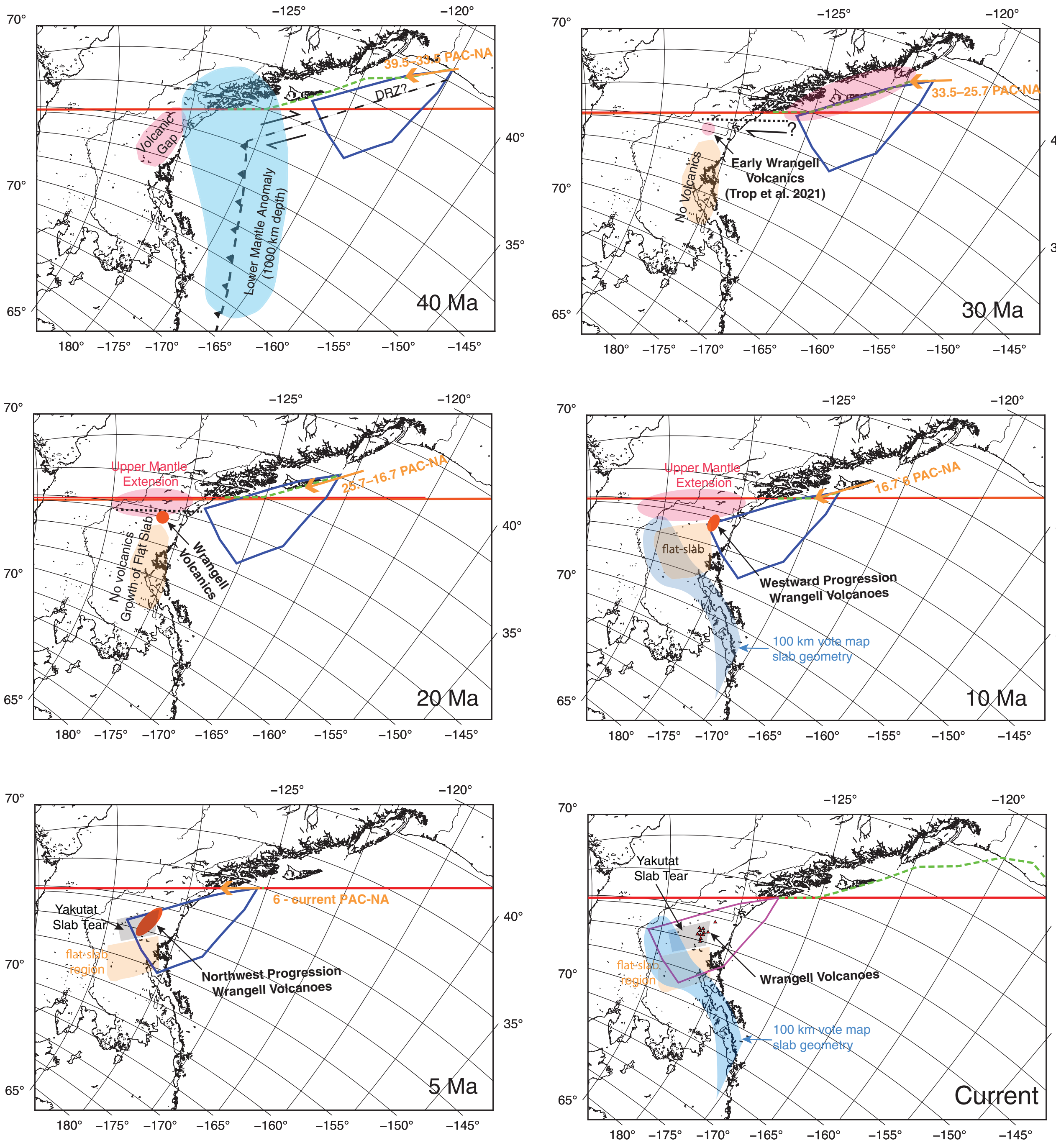

Figure 8.15 Kinematic model interpretation of EarthScope TA imaging results. The figure is set of six panels with a common base map created from an oblique Mercator projection comparable to Figures 8.12–8.14. The focus of each panel is the Yakutat polygon defined by G. L. Pavlis et al. (2019) backprojected to the time defined in the lower left corner of each panel using the plate model of Doubrovine and Tarduno (2008) for Pacific–North America relative motion. Each frame also shows a dashed green line that is the track of the Yakutat–Pacific–North American triple junction used as the anchor by G. L. Pavlis et al. (2019) for the backprojected polygon. The time of each frame was chosen as round numbers falling within each of the stage poles defined in the plate model. For each frame, we use an orange arrow to illustrate the relative motion within each stage. Each frame has interpretative overlay text and polygons discussed in the text.

As noted earlier, kinematics require that the Yakutat tear is bounded by the range of 13–6 Ma with 7–9 Ma being the most consistent with the new data. That suggests the tear initiated before the plate motion change at 6 Ma. We suggest, however, that the change at 6 Ma may have been a factor in the development of the tear. The eastward shift in Pacific Plate motion likely created the opposite effect we suggested for the 20 and 10 Ma panels. That is, instead of upper mantle extension, the eastern edge of the subducting slab would experience compression that contributed to the development of the tear we see today.

ACKNOWLEDGMENTS

This chapter grew out of discussions at the UNAVCO Alaska EarthScope and Beyond Virtual Seminar Series in Spring 2021 and the paired EarthScope Alaska and Beyond Virtual Workshop in May 2021, which were supported by the National Science Foundation and the National Aeronautics and Space Administration. The authors thank conference organizers Jeffrey Freymueller, Julie Elliot, Sarah Roeske, and Rick Aster, as well as participants at the meeting for thoughtful discussions. Sincere thanks to Tao Guo for sending us digital copies of the imaging results from their paper. This work was supported by NSF CAREER Award NSF-EAR 1945513 awarded to M. Jadamec, startup funding at Purdue University to X. Yang, NSF-EAR 1942431 to S. S. Wei, NSF EAR-2053042808 and Woods Hole Oceanographic Institution OBS Instrument Center Postdoctoral Scholarship to M. E. Mann, and NSF EAR-1829401 to K. M. Fischer. Maps were made with GMT (Wessel et al., 2013, 2019). Three-dimensional visualizations were produced with paraview (https://www.paraview.org).

AUTHOR CONTRIBUTIONS

G. Pavlis developed and completed the vote map analysis and did the visualization analysis with paraview. G. Pavlis and M. Jadamec wrote the bulk of the text of the chapter. All other authors contributed to the text through editing of the text and critical discussion of the interpretations. All authors were deeply involved in the progressive development of ideas described in the chapter.

AVAILABILITY STATEMENT

The software libraries we used to build the structured, 3-D grids for our analysis can be found on github at URL: https://github.com/pavlis/parallel_pwmig. That package is focused on imaging but contains a python library that can be used to convert EMC files to paraview "vts" files. All the collected earth models were converted to files directly loadable by the open-source visualization package called paraview (https://www.paraview.org) in the same (Cartesian) coordinate system as the paraview format files in the supplement of G. L. Pavlis et al. (2019). All the files used for paraview visualizations, a file containing the vote map field data, and the animation and pdf files noted in the text can be found on the companion website.

REFERENCES

Arrial, P., Billen, M. I. (2013). Influence of geometry and eclogitization on oceanic plateau subduction. *Earth and Planetary Science Letters*, *363*, 34–43.

Bauer, M. A., Pavlis, G. L., & Landes, M. (2014). Subduction geometry of the Yakutat Terrane, southeastern Alaska. *Geosphere (Boulder, CO)*, *11*(1), 201.

Bellahsen, N., Faccenna, C., & Funiciello, F. (2005). Dynamics of subduction and plate motion in laboratory experiments: Insights into the "plate tectonics" behavior of the Earth. *Journal of Geophysical Research*, *110* (B01401). doi: 10.1029/2004JB002999

Berkelhammer, S. E., Brueseke, M. E., Benowitz, J. A., Trop, J. M., Davis, K., Layer, P. W., & Weber, M. (2019). Geochemical and geochronological records of tectonic changes along a flat-slab arc-transform junction: Circa 30 Ma to ca. 19 Ma Sonya Creek volcanic field, Wrangell Arc, Alaska. *Geosphere (Boulder, CO)*, *15*(5), 1508–1538.

Billen, M. I. (2008). Modeling the dynamics of subducting slabs. *Annual Reviews of Earth and Planetary Sciences*, *36*, 325–356.

Billen, M. I., & Hirth, G. (2007). Rheological controls on slab dynamics. *Geochemistry Geophysics Geosystems*, *8* (Q08012). doi: 10.1029/2007GC001597

Bird, P. (2003). An updated digital model of plate boundaries. *Geochemistry Geophysics Geosystems*, *4*(3), 1027. doi: 10.1029/2001GC000252

Bostock, M. G., Rondenay, S., & Shragge, J. (2001). Multiparameter two-dimensional inversion of scattered teleseismic body waves 1. Theory for oblique incidence. *Journal of Geophysical Research*, *106*(B12), 771.

Boyce, A., Liddell, M. V., Pugh, S., Brown, J., McMurchie, E., Parsons, A., et al. (2023). A New P-Wave Tomographic Model (CAP22) for North America: implications for the subduction and cratonic metasomatic modification history of western Canada and Alaska. *Journal of Geophysical Research: Solid Earth*, *128*(3). doi: https://doi.org/10.1029/2022JB025745

Boyd, T., & Creager, K. (1991). The geometry of Aleutian subduction: Three dimensional seismic imaging. *Journal of Geophysical Research*, *96*(B2), 2267–2291.

Brocher, T. M., Fuis, G. S., Fisher, M. A., Plafker, G., Taber, J. J., & Christensen, N. I. (1994). Mapping the megathrust beneath the northern Gulf of Alaska using wide-angle seismic data. *Journal of Geophysical Research*, *99*(B6), 11663–11685.

Brueseke, M. E., Benowitz, J. A., Trop, J. M., Davis, K. N., Berkelhammer, S. E., Layer, P. W., & Morter, B. K. (2019). The Alaska Wrangell Arc: ~30 Ma of subduction-related magmatism along a still active arc-transform junction. *Terra Nova*, *31*(1), 59–66.

Bruns, T. R. (1983). Model for the origin of the Yakutat Block, an accreting terrane in the northern Gulf of Alaska. *Geology*, *11*(12), 718–721.

Burdick, S., Li, C., Martynov, V., Cox, T., Eakins, J., Mulder, T., et al. (2008). Upper mantle heterogeneity beneath North America from travel time tomography with global and USArray transportable array data. *Seismological Research Letters*, *79*(3), 384–392.

Burdick, S., van der Hilst, R. D., Vernon, F. L., Martynov, V., Cox, T., Eakins, J., et al. (2009). Model update December 2008: Upper mantle heterogeneity beneath North America from P-wave travel time tomography with global and USArray transportable array data. *Seismological Research Letters*, *80*(4), 638–645.

Burdick, S., van der Hilst, R. D., Vernon, F. L., Martynov, V., Cox, T., Eakins, J., et al. (2010). Model update January 2010: Upper mantle heterogeneity beneath North America from traveltime tomography with global and USArray transportable array data. *Seismological Research Letters*, *81*(5), 689–693.

Burdick, S., van der Hilst, R. D., Vernon, F. L., Martynov, V., Cox, T., Eakins, J., et al. (2012). Model update March 2011: Upper mantle heterogeneity beneath North America from traveltime tomography with global and USArray transportable array data. *Seismological Research Letters*, *83*(1), 23–28.

Burdick, S., van der Hilst, R. D., Vernon, F. L., Martynov, V., Cox, T., Eakins, J., et al. (2014). Model update January 2013: Upper mantle heterogeneity beneath North America from travel-time tomography with global and USArray transportable array data. *Seismological Research Letters*, *85*(1), 77–81.

Burdick, S., Vernon, F. L., Martynov, V., Eakins, J., Cox, T., Tytell, J., et al. (2017). Model update may 2016: Upper-mantle heterogeneity beneath North America from travel-time tomography with global and USArray data. *Seismological Research Letters*, *88*(2A), 319–325.

Burkett, E. R., & Billen, M. I. (2010). Three-dimensionality of slab detachment due to ridge-trench collision: Laterally simultaneous boudinage versus tear propagation. *Geochemistry, Geophysics, Geosystems*, *11*(11).

Capitanio, F., & Faccenda, M. (2012). Complex mantle flow around heterogeneous subducting oceanic plates. *Earth and Planetary Science Letters*, *353*, 29–37.

Christensen, D. H., & Beck, S. L. (1994). The rupture process and tectonic implications of the great 1964 Prince William Sound earthquake. *Pure and Applied Geophysics*, *142*(1), 29–53.

Christeson, G. L., Gulick, S. P. S., van Avendonk, H. J. A., Worthington, L. L., Reece, R. S., & Pavlis, T. L. (2010). The Yakutat Terrane: Dramatic change in crustal thickness across the Transition Fault, Alaska. *Geology (Boulder)*, *38*(10), 895–898.

Dahm, H. H., Gao, S. S., Kong, F., & Liu, K. H. (2017). Topography of the mantle transition zone discontinuities beneath Alaska and its geodynamic implications: Constraints from receiver function stacking. *Journal of Geophysical Research: Solid Earth*, *122*(12), 352.

DeMets, C., Gordon, R. G., Argus, D. F., & Stein, S. (1994). Effect of recent revisions to the geomagnetic reversal time scale on estimates of current plate motions. *Geophysical Research Letters*, *218*(207-237), 2191–2194.

Dickinson, W. R., & Snyder, W. S. (1979). Geometry of triple junctions related to San Andreas transform. *Journal of Geophysical Research*, *84*(B2), 561–572.

Doubrovine, P. V., & Tarduno, J. A. (2008). A revised kinematic model for the relative motion between Pacific oceanic plates and North America since the Late Cretaceous. *Journal of Geophysical Research*, *113*(B12).

Eberhart-Phillips, D., Christensen, D. H., Brocher, T. M., Hansen, R., Ruppert, N. A., Haeussler, P. J., & Abers, G. A. (2006). Imaging the transition from Aleutian subduction to Yakutat collision in central Alaska, with local earthquakes and active source data. *Journal of Geophysical Research*, *111* (B11303). doi: 10.1029/2005JB004240

Elliott, J., & Freymueller, J. T. (2020). A block model of present-day kinematics of Alaska and western Canada. *Journal of Geophysical Research: Solid Earth*, *125*(7), e2019JB018378.

Elliott, J. L., Larsen, C. F., Freymueller, J. T., & Motyka, R. J. (2010). Tectonic block motion and glacial isostatic adjustment in southeast Alaska and adjacent Canada constrained by GPS measurements. *Journal of Geophysical Research*, *115*(B9).

Engebretson, D. C., Cox, A., & Gordon, R. G. (1984). Relative motions between oceanic plates of the Pacific Basin. *Journal of Geophysical Research*, *89*(B12), 291.

Engebretson, D. C., Cox, A., & Gordon, R. G. (1985). Relative motions between oceanic and continental plates in the Pacific Basin. *Geological Society of America Special Paper*, *206*, 59 p.

Enkelmann, E., Zeitler, P., Garver, J., Pavlis, T., & Hooks, B. (2010). The thermochronological record of tectonic and surface process interaction at the Yakutat–North American collision zone in southeast Alaska. *American Journal of Science*, *310*(4), 231–260.

Esteve, C., Audet, P., Schaeffer, A. J., Schutt, D., Aster, R. C., & Cubley, J. (2020). The upper mantle structure of northwestern Canada from teleseismic body wave tomography. *Journal of Geophysical Research: Solid Earth*, *125*(2).

Esteve, C., Gosselin, J., Audet, P., Schaeffer, A. J., Schutt, D., & Aster, R. (2021). Surface-wave tomography of the Northern Canadian Cordillera Using Earthquake Rayleigh Wave Group Velocities. *Journal of Geophysical Research*, *126*.

Esteve, C., Schaeffer, A. J., & Audet, P. (2019). Upper mantle structure underlying the diamondiferous Slave Craton from teleseismic body-wave tomography. *Tectonophysics*, *757*, 187–202.

Fan, C., Pavlis, G. L., & Tuncay, K. (2006). GCLgrid: A three-dimensional geographical curvilinear grid library for computational seismology. *Computers and Geosciences*, *32*(3), 371–381.

Ferris, A., Abers, G. A., Christensen, D. H., & Veenstra, E. (2003). High resolution image of the subducted Pacific (?) Plate beneath central Alaska, 50-150 km depth. *Earth and Planetary Science Letters*, *214*(3–4), 575–588.

Finzel, E. S., Trop, J. M., Ridgway, K. D., & Enkelmann, E. (2011). Upper plate proxies for flat-slab subduction processes in southern Alaska. *Earth and Planetary Science Letters*, *303*(3–4), 348–360.

Fitzgerald, P. G., Roeske, S. M., Benowitz, J. A., Riccio, S. J., Perry, S. E., & Armstrong, P. A. (2014). Alternating asymmetric topography of the Alaska Range along the strike-slip Denali Fault: Strain partitioning and lithospheric control across a terrane suture zone. *Tectonics*, *8*, 1519–1533.

Fitzgerald, P. G., Sorkhabi, R. B., Redfield, T. F., & Stump, E. (1995). Uplift and denudation of the central Alaska Range: A case study in the use of apatite fission track thermochronology to determine absolute uplift parameters. *Journal of Geophysical Research*, *100*(B10), 20175–20191.

Fuis, G. S., Moore, T. E., Plafker, G., Brocher, T. M., Fisher, M. A., Mooney, W. D., et al. (2008). Trans-Alaska Crustal Transect and continental evolution involving subduction underplating and synchronous foreland thrusting. *Geology*, *36*(3), 267.

Fuston, S., & Wu, J. (2020). Raising the Resurrection Plate from an unfolded-slab plate tectonic reconstruction of northwestern North America since early Cenozoic time. *Geological Society of America Bulletin*, *133*(5–6), 1128–1140.

Gerya, T. (2011). Future directions in subduction modeling. *Journal of Geodynamics*, *52*(5), 344–378.

Global Volcanism Program. (2022). [database] volcanoes of the world (v. 5.0.1; 19 dec 2022). distributed by smithsonian institution [Database]. doi: https://doi.org/10.5479/si.GVP.VOTW5-2022.5.0

Goes, S., Agrusta, R., van Hunen, J., & Garel, F. (2017). Subduction-transition zone interaction: A review. *Geosphere*, *13*(3), 644–664.

Gou, T., Zhao, D., Huang, Z., & Wang, L. (2019). Aseismic deep slab and mantle flow beneath Alaska: Insight from anisotropic tomography. *Journal of Geophysical Research: Solid Earth*, *124*(2), 1700–1724.

Gudmundsson, O., & Sambridge, M. (1998). A regionalized upper mantle (RUM) seismic model. *Journal of Geophysical Research*, *103*(B4), 7121–7136.

Haeussler, P. J., Bradley, D. C., Wells, R. E., & Miller, M. L. (2003). Life and death of the Resurrection Plate; evidence for its existence and subduction in the northeastern Pacific in Paleocene-Eocene time. *Geological Society of America Bulletin*, *115*(7), 867–880.

Hanna, J., & Long, M. (2012). SKS splitting beneath Alaska: Regional variability and implications for subduction processes at a slab edge. *Tectonophysics*, *530–531*, 272–285.

Hayes, G., Moore, G. L., Portner, D. E., Hearne, M., Flamme, H., Furtney, M., & Smoczyk, G. M. (2018). Slab2, a comprehensive subduction zone geometry model. *Science*, *362*(6410), 58–61.

Hayes, G., Wald, D., & Johnson, R. (2012). Slab1. 0: A three-dimensional model of global subduction zone geometries. *Journal of Geophysical Research*, *117*(B1), B01302.

Haynie, K. L., & Jadamec, M. A. (2017). Tectonic drivers of the Wrangell block: Insights on forearc sliver processes from 3D geodynamic models of Alaska. *Tectonics*, *36*, 28.

Hults, C. P., Wilson, F. H., Donelick, R. A., & O'Sullivan, P. B. (2013). Two flysch belts having distinctly different provenance suggest no stratigraphic link between the Wrangellia composite terrane and the paleo-Alaskan margin. *Lithosphere*, *5*(6), 575–594.

Jadamec, M. A. (2016). Insights on slab-driven mantle flow from advances in three-dimensional modelling. *Journal of Geodynamics*, *100*, 51–70.

Jadamec, M. A., & Billen, M. I. (2010). Reconciling surface plate motions and rapid three-dimensional flow around a slab edge. *Nature*, *465*, 338–342.

Jadamec, M. A., & Billen, M. I. (2012). The role of rheology and slab shape on rapid mantle flow: Three-dimensional numerical models of the Alaska slab edge. *Journal of Geophysical Research*, *117* (B02304).

Jadamec, M. A., Billen, M. I., & Roeske, S. M. (2013). Three-dimensional numerical models of flat slab subduction and the Denali fault driving deformation in south-central Alaska. *Earth and Planetary Science Letters*, *376*, 29–42.

Jadamec, M. A., Kreylos, O., Chang, B., Fischer, K. M., & Yikilmaz, M. B. (2018a). Movies for: A visual survey of global slab geometries with ShowEarthModel and implications for a three-dimensional subduction paradigm. *Earth and Space Science (Digital Collection hosted at the University at Buffalo Institutional Repository (UBIR))*, Movie Downloads: http://hdl.handle.net/10477/76912. Movie Streams: http://goo.gl/Y7PDEX.

Jadamec, M. A., Kreylos, O., Chang, B., Fischer, K. M., & Yikilmaz, M. B. (2018b). A visual survey of global slab geometries with ShowEarthModel and implications for a three-dimensional subduction paradigm. *Earth and Space Science*, *5*, 18.

Jarrard, R. D. (1986). Relations among subduction parameters. *Reviews of Geophysics*, *24*(2), 217–284.

Jiang, C., Schmandt, B., Hansen, S. M., Dougherty, S. L., Clayton, R. W., Farrell, J., & Lin, F.-C. (2018). Rayleigh and S wave tomography constraints on subduction termination and lithospheric foundering in Central California. *Earth and Planetary Science Letters*, *488*, 14–26.

Jiang, C., Schmandt, B., Ward, K. M., Lin, F.-C., & Worthington, L. L. (2018). Upper mantle seismic structure of Alaska from Rayleigh and S-wave tomography. *Geophysical Research Letters*, *45*(19), 10350–10359.

Kalbas, J. L., Freed, A. M., & Ridgway, K. D. (2008). Contemporary fault mechanics in southern Alaska. *Geophysical Monograph Series*, *179*, 321–336.

Kim, Y. H., Abers, G. A., Li, J., Christensen, D., Calkins, J., & Rondenay, S. (2014). Alaska megathrust 2: Imaging the megathrust zone and Yakutat/Pacific Plate interface in the Alaska subduction zone. *Journal of Geophysical Research: Solid Earth*, *119*(3), 1924–1941.

Koons, P. O., Hooks, B., Pavlis, T., Upton, P., & Barker, A. (2010). Three-dimensional mechanics of Yakutat convergence in the southern Alaskan plate corner. *Tectonics*, *29*(4).

Kumar, P., Yuan, X., Kind, R., & Kosarev, G. (2005). The lithosphere-asthenosphere boundary in the Tien Shan-Karakoram region from S receiver functions: Evidence for continental subduction. *Geophysical Research Letters*, *32*(7).

Lallemand, S., Heuret, A., & Boutelier, D. (2005). On the relationships between slab dip, back-arc stress, upper plate absolute motion, and crustal nature in subduction zones. *Geochemistry Geophysics Geosystems*, *6*(9), Q09006.

Li, C., van der Hilst, R. D., Engdahl, E. R., & Burdick, S. (2008). A new global model for P wave speed variations in Earth's mantle. *Geochemistry Geophysics Geosystems*, *9*(5).

Li, C., van der Hilst, R. D., & Toksoz, M. N. (2006). Constraining P-wave velocity variations in the upper mantle beneath southeast Asia. *Physics of the Earth and Planetary Interiors*, *154*(2), 180–195.

Lou, X., van der Lee, S., & Lloyd, S. (2013). AIMBAT: A Python/Matplotlib tool for measuring teleseismic arrival times. *Seismological Research Letters*, *84*(1), 85–93.

Madsen, J. K., Thorkelson, D. J., Friedman, R. M., & Marshall, D. D. (2006). Cenozoic to Recent plate configurations in the Pacific Basin; ridge subduction and slab window magmatism in western North America. *Geosphere*, *2*(1), 11–34.

Manea, V. C., Perez-Gussinye, M., & Manea, M. (2012). Chilean flat slab subduction controlled by overriding plate thickness and trench rollback. *Geology*, *40*(1), 35–38.

Mann, M. E., Abers, G. A., Daly, K. A., & Christensen, D. H. (2022). Subduction of an oceanic plateau across southcentral Alaska: Scattered-wave imaging. *Journal of Geophysical Research: Solid Earth*, *127*(1).

Martinod, J., Funiciello, F., Faccenna, C., Labanieh, S., & Regard, V. (2005). Dynamical effects of subducting ridges: Insights from 3D laboratory models. *Geophysical Journal International*, *163*, 1137–1150.

Mason, W. G., Moresi, L., Betts, P. G., & Miller, M. S. (2010). Three-dimensional numerical models of the influence of a buoyant oceanic plateau on subduction zones. *Tectonophysics*, *483*, 71–79.

McClelland, W. C., Strauss, J. V., Colpron, M., Gilotti, J. A., Faehnrich, K., Malone, S. J., et al. (2021). 'Taters versus sliders; evidence for a long-lived history of strike-slip displacement along the Canadian Arctic transform system (CATS). *GSA Today*, *31*(7), 4–11.

McPherson, A., Christensen, D., Abers, G., & Tape, C. (2020). Shear wave splitting and mantle flow beneath Alaska. *Journal of Geophysical Research: Solid Earth*, *125*(4), e2019JB018329.

Moore, T. E., & Box, S. E. (2016). Age, distribution and style of deformation in Alaska north of 60 N: Implications for assembly of Alaska. *Tectonophysics*, *691*, 133–170.

Morra, G., Regenauer-Lieb, K., & Giardini, D. (2006). Curvature of oceanic arcs. *Geology*, *34*(10), 877–880.

Müller, R. D., Sdrolias, M., Gaina, C., & Roest, W. R. (2008). Age, spreading rates, and spreading asymmetry of the world's ocean crust. *Geochemistry Geophysics Geosystems*, *9*(4).

Müller, R. D., Zahirovic, S., Williams, S. E., Cannon, J., Seton, M., Bower, D. J., et al. (2019). A global plate model including lithospheric deformation along major rifts and orogens since the Triassic. *Tectonics*, *38*(6), 1884–1907.

Nayak, A., Eberhart-Phillips, D., Ruppert, N. A., Fang, H., Moore, M. M., Tape, C., et al. (2020). 3-D seismic velocity models for alaska from joint tomographic inversion of body-wave and surface-wave data. *Seismological Research Letters*, *91*(6), 3106–3119.

Pavlis, G. L., Bauer, M. A., Elliott, J. L., Koons, P., Pavlis, T. L., Ruppert, N., et al. (2019). A unified three-dimensional model of the lithospheric structure at the subduction corner in southeast Alaska; summary results from STEEP. *Geosphere (Boulder, CO)*, *15*(2), 382–406.

Pavlis, T. L., Amato, J. M., Trop, J. M., Ridgway, K. D., Roeske, S. M., & Gehrels, G. E. (2019). Subduction polarity in ancient arcs; a call to integrate geology and geophysics to decipher the Mesozoic tectonic history of the Northern Cordillera of North America. *GSA Today*, *29*(11), 4–10.

Plafker, G., & Berg, H. C. (1994). Overview of the geology and tectonic evolution of Alaska. In *DNAG, Geology of North America; The Geology of Alaska* (Vol. G-1). Geological Society of America.

Plafker, G., Gilpin, L. M., & Lahr, J. C. (1994). Plate 12: Neotectonic Map of Alaska. In G. Plafker & H. Berg (Eds.), *DNAG, The Geology of North America; The Geology of Alaska* (Vol. G1). Geological Society of America.

Plafker, G., Moore, J. C., & Winkler, G. R. (1994). Geology of the southern Alaska margin. In G. Plafker & H. Berg (Eds.), *DNAG, Geology of North America; The Geology of Alaska* (Vol. G-1). Geological Society of America.

Products, I. D. (2021, Aug). *Data services products: Emc iris earth model collaboration*. Incorporated Research Institution for Seismology. Retrieved from http://ds.iris.edu/ds/products/emc/

Pysklywec, R. N., & Ishii, M. (2005). Time dependent subduction dynamics driven by the instability of stagnant slabs in the transition zone. *Physics of Earth and Planetary Interiors*, *149*, 115–132.

Ratchkovski, N. A., & Hansen, R. A. (2002a). New constraints on tectonics of interior Alaska: Earthquake locations, source mechanisms, and stress regime. *Bulletin of the Seismological Society of America*, *92*(3), 998–1014.

Ratchkovski, N. A., & Hansen, R. A. (2002b). New evidence for segmentation of the Alaska subduction zone. *Bulletin of the Seismological Society of America*, *92*(5), 1754–1765.

Regan, S. P., Benowitz, J. A., & Holland, M. E. (2020, February). A plutonic brother from another magma mother: Disproving the Eocene Foraker-McGonagall pluton piercing point and implications for long-term slip on the Denali Fault. *Terra Nova*, *32*, 66–74. doi: 10.1111/TER.12437

Richter, D. H., Smith, J. G., Lanphere, M. A., Dalrymple, G. B., Reed, B. L., & Shew, N. (1990). Age and progression of volcanism, Wrangell volcanic field, Alaska. *Bulletin of Volcanology*, *53*(1), 29–44.

Schellart, W. P., Freeman, J., Stegman, D. R., Moresi, L., & May, D. (2007). Evolution and diversity of subduction zones controlled by slab width. *Nature*, *446*, 308–311. doi: 10.1038

Schellart, W. P., Stegman, D., & Freeman, J. (2008). Global trench migration velocities and slab migration induced upper mantle volume fluxes: Constraints to find an Earth reference frame based on minimizing viscous dissipation. *Earth-Science Reviews*, *88*, 118–144.

Seton, M., Müller, R. D., Zahirovic, S., Williams, S., Wright, N. M., Cannon, J., et al. (2020). A global data set of present-day oceanic crustal age and seafloor spreading parameters. *Geochemistry, Geophysics, Geosystems*, *21*(10), e2020GC009214.

Sharples, W., Jadamec, M. A., Moresi, L. N., & Capitanio, F. (2014). Overriding plate controls on subduction evolution. *Journal of Geophysical Research*, *119*, 6684–6704. doi: 10.1002/2014JB011163

Shephard, G. E., Matthews, K. J., Hosseini, K., & Domeier, M. (2017). On the consistency of tomographically imaged lower mantle slabs. *Geophysical Research Abstracts*, *19*, @Abstract EGU2017 – 7916.

Sobolev, S., & Babeyko, A. (2005). What drives orogeny in the Andes? *Geology*, *33*(8), 617.

Stephens, C. D., Fogleman, K. A., Lahr, J. C., & Page, R. A. (1984). The Wrangell Benioff zone, southern Alaska. *Geology*, *12*, 373–376.

Syracuse, E. M., & Abers, G. A. (2006). Global compilation of variations in slab depth beneath arc volcanoes and implications. *Geochemistry Geophysics Geosystems*, *7*(5), Q05017. doi: 10.1029/2005GC001045

Thorkelson, D. J. (1996). Subduction of diverging plates and the principles of slab window formation. *Tectonophysics*, *255*(1–2), 47–63.

Tozer, B., Sandwell, D. T., Smith, W. H., Olson, C., Beale, J., & Wessel, P. (2019). Global bathymetry and topography at 15 arc sec: SRTM15+. *Earth and Space Science*, *6*(10), 1847–1864.

Trop, J. M., Benowitz, J. A., Kirby, C. S., & Brueseke, M. E. (2021). Geochronology of the Wrangell Arc; spatial-temporal evolution of slab-edge magmatism along a flat-slab, subduction-transform transition, Alaska-Yukon. *Geosphere*, *18*(1), 19–48.

VanDecar, J. C., James, D. E., & Assumpcao, M. (1995). Seismic evidence for a fossil mantle plume beneath South America and implications for plate driving forces. *Nature*, *378*(6552), 25–31.

van Hunen, J., van den Berg, A. P., & Vlaar, N. J. (2004). Various mechanisms to induce present-day shallow flat subduction and implications for the younger earth: A numerical parameter study. *Physics of the Earth and Planetary Interiors*, *146*(1), 179–194.

van Stiphout, A. M., Cottaar, S., & Deuss, A. (2019). Receiver function mapping of mantle transition zone discontinuities beneath Alaska using scaled 3-D velocity corrections. *Geophysical Journal International*, *219*(2), 1432–1446.

Veilleux, A. M., & Doser, D. I. (2007). Studies of Wadati-Benioff zone seismicity of the Anchorage, Alaska, region. *Bulletin of the Seismological Society of America*, *97*(1B), 52–62.

Wallace, W., & Engebretson, D. (1984). Relationships between plate motions and Late Cretaceous to Paleogene magmatism in southwestern Alaska. *Tectonics*, *3*(2), 295–315.

Wang, J., & Zhou, D. (2008). P-wave anisotropic tomography beneath northeast Japan. *Physics Earth and Planetary Interiors*, *170*, 115–133. doi: https://doi.org/10.1016/j.pepi.2008.07.042

Wang, J., & Zhou, D. (2013). P-wave tomography for 3-D radial and azimuthal anisotropy of Tohoku and Kyushu subduction zones. *Geophysical Journal International*, *193*, 1166–1181. doi: https://doi.org/10.1093/gji/ggt086

Wells, R., Bukry, D., Friedman, R., Pyle, D., Duncan, R., Haeussler, P., & Wooden, J. (2014). Geologic history of Siletzia, a large igneous province in the Oregon and Washington Coast Range; correlation to the geomagnetic polarity time scale and implications for a long-lived Yellowstone Hotspot. *Geosphere (Boulder, CO)*, *10*(4), 692–719.

Wessel, P., Luis, J., Uieda, L., Scharroo, R., Wobbe, F., Smith, W. H., & Tian, D. (2019). The generic mapping tools version 6. *Geochemistry, Geophysics, Geosystems*, *20*(11), 5556–5564.

Wessel, P., Smith, W. H., Scharroo, R., Luis, J., & Wobbe, F. (2013). Generic mapping tools: Improved version released. *Eos, Transactions American Geophysical Union*, *94*(45), 409–410.

Worthington, L. L., Gulick, S. P. S., & Pavlis, T. L. (2008). Identifying active structures in the Kayak Island and Pamplona zones; implications for offshore tectonics of the Yakutat Microplate, Gulf of Alaska. *Geophysical Monograph*, *179*, 257–268.

Worthington, L. L., Van Avendonk, H. J. A., Gulick, S. P. S., Christeson, G. L., & Pavlis, T. L. (2012). Crustal structure of the Yakutat terrane and the evolution of subduction and collision in southern Alaska. *Journal of Geophysical Research*, *117*(B1).

Wu, J., Suppe, J., Lu, R., & Kanda, R. (2016). Philippine Sea and East Asian plate tectonics since 52 Ma constrained by new subducted slab reconstruction methods. *Journal of Geophysical Research: Solid Earth*, *121*(6), 4670–4741. doi: https://doi.org/10.1002/2016JB012923

Yang, X., & Gao, H. (2020). Segmentation of the Aleutian-Alaska subduction zone revealed by full-wave ambient noise tomography: Implications for the along-strike variation of volcanism. *Journal of Geophysical Research: Solid Earth*, *125*, 1–20. doi: 10.1029/2020JB019677

Zhao, D., Christensen, D., & Pulpan, H. (1995). Tomographic imaging of the Alaska subduction zone. *Journal of Geophysical Research*, *100*(B4), 6487–6504.

Zhao, D., Yanada, T., Hasegawa, A., Umino, N., & Wei, W. (2012). Imaging the subducting slabs and mantle upwelling under the Japan Islands. *Geophysical Journal International*, *190*(2), 816–828.